

Notice

This manuscript has been peer reviewed. This version submitted to EarthArXiv is the final submitted version prior to acceptance. The official published version and this one will differ due to copy editing, typesetting, and formatting, but not in terms of scientific content and results.

This publication can be referenced as

Heimisson, E. R., & Segall, P. (2020). Physically consistent modeling of dike induced deformation and seismicity: Application to the 2014 Bárðarbunga dike, Iceland. *Journal of Geophysical Research: Solid Earth*, 125 <https://doi.org/10.1029/2019JB018141>

1 **Physically consistent modeling of dike induced**
2 **deformation and seismicity: Application to the 2014**
3 **Bárðarbunga dike, Iceland**

4 **Elías R. Heimisson^{1*}, Paul Segall¹**

5 ¹Department of Geophysics, Stanford University, Stanford, California, USA

6 **Key Points:**

- 7 • The model captures the complex space-time history of seismicity and deformation.
- 8 • Results are consistent with dike induced earthquakes being triggered on pre-existing
- 9 faults.
- 10 • Magma pressure increases when the dike stops, but drops rapidly as it propagates.

*Now at: Seismological Laboratory, California Institute of Technology, Pasadena, California, USA

Corresponding author: Elías R. Heimisson, eliasrh@stanford.edu, eheimiss@caltech.edu

Abstract

Dike intrusions are often associated with surface deformation and propagating swarms of earthquakes. These are understood to be manifestations of the same underlying physical process, although rarely modeled as such. We construct a physics-based model of the 2014 Bárðarbunga dike, by far the best observed large dike ($> 0.5 \text{ km}^3$) to date. We constrain the background stress state by the total dike deformation, the time-dependent dike pressure from continuous GPS and the extent of the seismic swarm, and the spatial dependence of frictional properties via the space-time evolution of seismicity. We find that the geodetic and earthquake data can be reconciled with a self-consistent set of parameters. The complex spatial and temporal evolution of the Bárðarbunga seismicity can be explained by dike-induced elastic stress changes on preexisting faults, constrained by observed focal mechanisms. In particular, the model captures the segmentation of seismicity, where only the newest dike segment is seismically active. Our results indicate that many features of the seismicity result from the interplay between time-dependent magma pressure within the dike and stress memory effects. The spatial variability in seismicity requires heterogeneity in frictional properties and/or local initial stresses. Modeling suggests that the dike pressure drops during rapid advances and increases during pauses, which primarily causes the segmentation of the seismicity. Joint analysis of multiple data types could potentially lead to improved, physics-based eruption forecasts.

1 Introduction

A propagating dike deforms the crust and causes dramatic stress changes in the near field; this usually results in a propagating swarm of seismicity. It is generally thought that the leading edge of the seismicity marks the approximate location of the dike tip since that is where the local stresses are largest. The September 1977 Krafla, Iceland dike intrusion provides convincing evidence for seismicity being produced near the dike tip. Dike propagation was marked by a swarm of seismicity that migrated $\sim 8 \text{ km}$ from the center of the Krafla caldera, eventually intersecting a geothermal well [*Brandsdottir and Einarsson, 1979*]. A small volume of basaltic tephra erupted from the borehole [*Larsen and Grönvold, 1979*], shortly after the earthquakes propagated into the vicinity of the well. Despite this clear association, the exact mechanism of dike-induced seismicity is not completely understood.

42 Seismicity and deformation have long been successfully used to study, and even fore-
43 cast, volcanic processes. Yet, most studies do not jointly model the two types of data
44 quantitatively, although they are usually considered signatures of the same underlying
45 process. Modeling deformation in volcanic settings is reasonably well understood on short
46 time scales when elastic deformation predominates. However, modeling earthquake pro-
47 duction or seismicity rate in response to stress changes is currently a subject of active
48 research. Here we investigate seismicity triggered by a propagating dike into a critically
49 stressed and faulted rift-zone. We thus expect that seismicity should manifest as slip on
50 pre-existing faults, which can be described by a rate-and-state based seismicity model
51 law [Segall *et al.*, 2013]. This approach contrasts with models that describe damage ac-
52 cumulation in formerly un-faulted crust [e.g. Got *et al.*, 2017]. To gain further insight
53 into dynamic, and sometimes life-threatening, earth processes we seek to develop quan-
54 titative models that are consistent with more than one independent data type. The goal
55 of this study is to develop such a model and apply it to the 2014 Bárðarbunga dike in-
56 trusion, with fully consistent deformation and stress fields that affect both GPS, InSAR,
57 and seismicity data. Such a framework could potentially lead to improved, physics-based
58 eruption forecasts.

59 Most studies of dike-induced deformation apply kinematic dislocation models [e.g.
60 Du and Aydin, 1992; Jónsson *et al.*, 1999; Sigmundsson *et al.*, 2015; Green *et al.*, 2015].
61 These models are subject to *ad hoc* regularization to smooth the dike opening, where the
62 degree of smoothing is based on signal to noise ratio of the data, not the physics of pres-
63 surized cracks. A different approach to modeling magmatic intrusions is to derive open-
64 ing from traction boundary conditions [e.g. Cayol and Cornet, 1998; Yun *et al.*, 2006;
65 Sigmundsson *et al.*, 2010; Hooper *et al.*, 2011; Segall *et al.*, 2013]. We refer to this a mag-
66 matic crack model since viscous stresses acting on the dike walls are neglected. This
67 approach greatly reduces the number of free parameters and results in a smoothly vary-
68 ing opening corresponding to a fluid-filled crack in static equilibrium with the crustal
69 stress state. An important benefit of this approach is that it yields more realistic stress
70 fields surrounding the dike, whereas kinematic dislocation models fail to accurately rep-
71 resent the near field stresses imposed by the dike.

72 Our study may be regarded as a test of the hypothesis that a physics-based dike
73 model, constrained by geodetic observations, can be reconciled with the complex spa-
74 tial and temporal evolution of seismicity during the 2014 Bárðarbunga dike intrusion us-

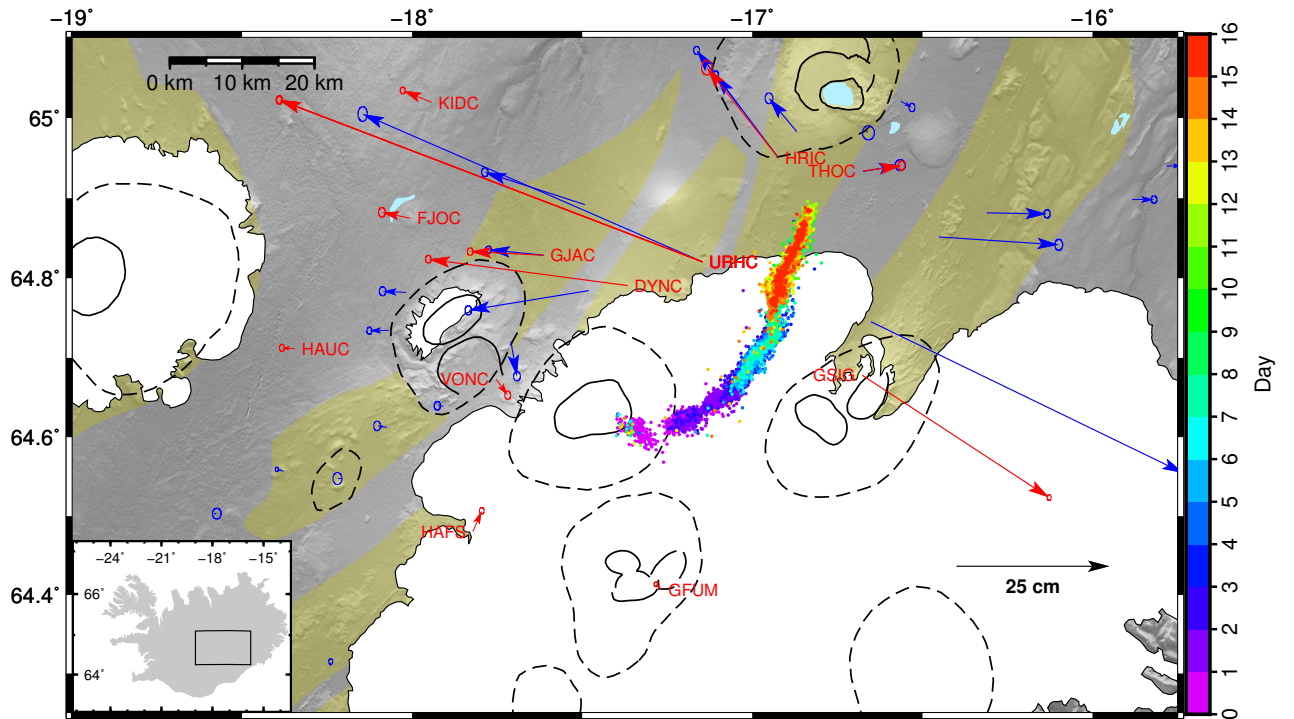
75 ing an earthquake production law based on rate-and-state friction [*Dieterich, 1994; Heimis-*
76 *son and Segall, 2018*]. Specifically, we hypothesize that seismicity is triggered on pre-
77 stressed faults that host a population of seismic sources with heterogeneous initial con-
78 ditions. Our findings suggest that these models are in general agreement with observa-
79 tions.

80 *Segall et al. [2013]* took the first step toward a joint quantitative analysis of micro-
81 seismicity and surface deformation during dike propagation. They performed a joint in-
82 version of data from the 2007 "Father's Day" intrusion in Kilauea. Using a boundary
83 element crack model, they related dike opening to surface displacements and changes in
84 stresses in volume elements (voxels) surrounding the dike. From the predicted shear and
85 normal tractions, acting on fault planes inside each voxel, the cumulative number of events
86 was computed using the *Dieterich [1994]* seismicity rate theory. In a broad sense, we ap-
87 ply the same approach to the Bárðarbunga dike, however the Bárðarbunga dike was much
88 larger and better monitored than Father's Day intrusion, with a more complicated spa-
89 tial and temporal evolution. This resulted in a much richer and more complete data set.
90 For example, the Bárðarbunga dike was monitored by nearly a dozen continuous GPS
91 stations (Figure 1), InSAR acquisitions, and a dense seismic network which was used to
92 locate over 30,000 events with high accuracy [*Ágústsdóttir et al., 2016*]. In contrast, the
93 Father's Day intrusion only had a few hundred located events. Because of the non-planar
94 geometry of the Bárðarbunga dike we discretize the surrounding crust into tetrahedral
95 voxels. Furthermore, we allow the dike to evolve vertically, as well as laterally, in a re-
96 alistic tectonic stress field; in contrast the height of the Fathers Day dike was fixed.

97 In section 2, we discuss how we construct the dike model, and the numerical strat-
98 egy for computing the dike opening and model predicted seismicity. In section 3, we dis-
99 cuss a three-step inversion strategy and show the results of each step: First, we constrain
100 the crustal and magma densities and background stress field surrounding the dike us-
101 ing cumulative GPS and InSAR displacements. Second, we constrain the time-dependent
102 pressure in the dike using continuous GPS data. Third, we constrain parameters related
103 to the earthquake production law and simulate the earthquake catalog. Section 4 offers
104 a discussion of the results and model assumptions, and explains interesting phenomena
105 observed in the seismicity.

106 1.1 The 2014 Bárðarbunga dike, Iceland

107 The 2014 Bárðarbunga dike is by far the best instrumented large dike intrusion to
108 date, with more than 30,000 detected earthquakes [Ágústsdóttir *et al.*, 2016]. Large de-
109 formations were observed by continuous GPS and a number of InSAR acquisitions [*Sig-*
110 *mundsson et al.*, 2015]. The high-quality data led to the following observations: The seis-
111 micity was mostly concentrated in a limited depth range of 5 – 7 km, and segmented along
112 strike, with only the newest dike segment seismically active [Ágústsdóttir *et al.*, 2016] (Fig-
113 ure 1). In this paper we use the word *segmentation* in the same sense as *Sigmundsson*
114 *et al.* [2015]. The trajectory of the dike had several abrupt turns; propagation often halted
115 before changing direction. Continuous GPS data show that the dike inflated during these
116 pauses implying it accumulated magma [*Sigmundsson et al.*, 2015].



117 **Figure 1.** Location of the Bárðarbunga volcano, dike seismicity and net GPS displacements.
 118 Dashed lines mark individual central volcanoes, solid lines are caldera faults and yellow shaded
 119 areas are fissure swarms associated with central volcanoes. Vectors show cumulative displacement
 120 spanning the 2014 diking event. Red arrows, and labels, are continuous GPS stations used in the
 121 time-dependent inversion. Blue arrows are campaign GPS stations. Dots show dike seismicity
 122 from *Ágústsdóttir et al.* [2019], which are color-coded by days since the beginning of the intrusion.

123 The initial analysis of seismicity [*Sigmundsson et al.*, 2015] revealed some variabil-
 124 ity in focal mechanisms among the larger events, ranging from strike-slip to normal; most
 125 estimated focal mechanisms were significantly oblique. A later study by *Ágústsdóttir et al.*
 126 [2016] investigated focal mechanisms at the distal end (the last ~ 13 km) of the dike with
 127 a much denser network. They found the dominant focal mechanism (85% of analyzed
 128 events) to be strike-slip with the same strike and no significant volumetric component.
 129 Based on which nodal plane was better constrained by the data and the orientation of
 130 the regional stress field, they concluded that these are left-lateral events with strike 38°
 131 East of North. The dike in this region strikes 25° . The other common focal mechanisms
 132 in this region are right-lateral slip with a strike of $\sim 17^\circ$. These mechanisms tend to oc-

133 cur only behind the leading edge of the dike. Along the first 0 – 10 km of the dike the
 134 mechanisms are highly variable. From 10 – 30 km, the mechanisms appear to have sim-
 135 ilar strike as the end region ($\sim 38^\circ$), but are predominantly right-lateral. From 30 km
 136 to the end region the events are predominantly left lateral (see *Ágústsdóttir et al.* [2019]
 137 for details). We apply these inferred fault planes as prior constraints, as detailed in sec-
 138 tion 3.3.

139 *Sigmundsson et al.* [2015]; *Green et al.* [2015]; *Ruch et al.* [2016]; *Parks et al.* [2017]
 140 previously modeled the surface deformation due to the dike and the Bárðarbunga caldera
 141 collapse. However, most of the published studies have employed kinematic dislocation
 142 models. In contrast, in this study, we try to model realistic near field stresses. This is
 143 required to capture the temporally complex propagation of seismicity (Figure 1), and
 144 to accurately predict the cumulative number of earthquakes. In the following section,
 145 we describe the dike model in detail, along with a description of its limitations.

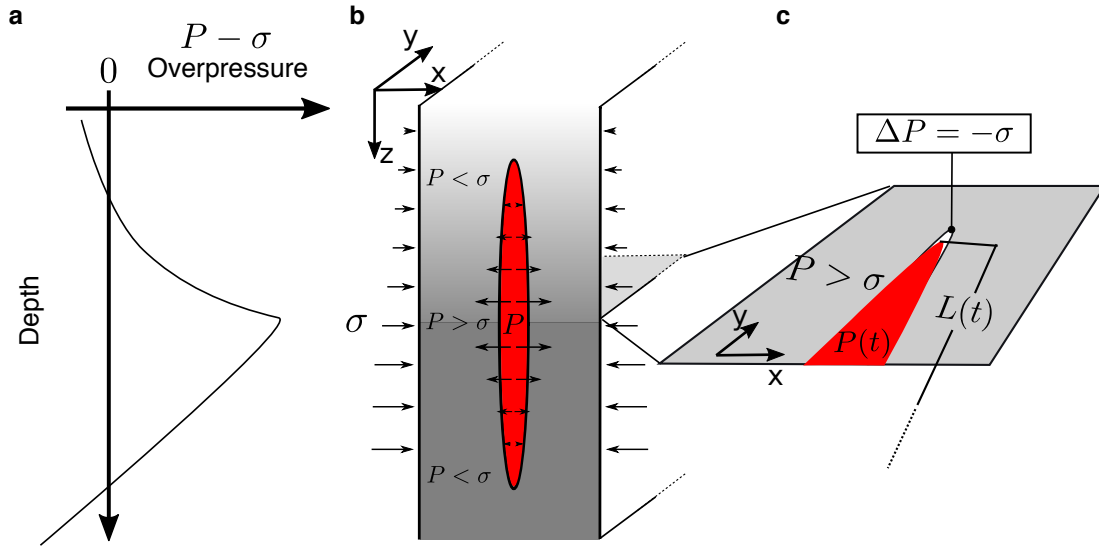
146 2 Methods

147 2.1 Dike model

148 Dike opening is controlled by the difference between the dike normal stress $\sigma =$
 149 $P_{litho} + \sigma_n$ and the magma pressure P ; the dike overpressure is $\Delta P = P - \sigma = P -$
 150 $(P_{litho} + \sigma_n)$ (Figure 2a-b). Here, P_{litho} is the lithostatic pressure and σ_n is the com-
 151 ponent of the tectonic stress field normal to the dike. The density of the crust varies with
 152 depth, and at shallow levels is typically less than the density of basaltic magma. The den-
 153 sity contrast can stabilize the dike vertically and promote lateral propagation [e.g. *Fi-*
 154 *alko and Rubin, 1999; Townsend et al., 2017*]. The depth where the density of the magma
 155 and crust is the same is referred to as the level of neutral buoyancy (LNB). This may
 156 not be where the maximum opening occurs, since that also depends on σ_n .

157 Near the top and bottom boundary of the dike the overpressure may change sign
 158 even though the dike opening is non-negative. Furthermore, at the laterally propagat-
 159 ing dike tip (Figure 2c) there is likely a magma-free cavity filled with pore-fluids from
 160 the crust or exsolved volatiles from the magma [*Rubin, 1993*]. The pressure inside the
 161 cavity is highly uncertain, but one end member case is that the cavity pressure is neg-
 162 ligible such that the overpressure there is $\Delta P \sim -\sigma$; this is assumed here (note $\Delta P <$
 163 0 is an *underpressure*). The length of the tip cavity can be solved for under the assump-

164 tion that the crack is non-singular, as described later. A cavity may exist at the top and
 165 bottom margins (Figure 2b) but the depth dependence of $P-\sigma$ results in a more grad-
 166 ual transition where the over pressure becomes negative, resulting in a non-singular crack
 167 tip without introducing a tip cavity (Figure 2a).



168 **Figure 2.** Schematic cross-section showing the depth dependent parameters that affect dike
 169 opening. a, Schematic overpressure profile within a vertical dike cross section. b, Schematic dike
 170 opening with both top and bottom tip under-pressured. The opening is idealized as elliptical,
 171 although that is not consistent with the overpressure profile. c, Dike tip at the lateral end with a
 172 crack tip cavity and length $L(t)$ defined as the distance to the front of the pressurized magma.

173 To attain realistic stresses in the near field, we simulate a non-singular crack. It
 174 is fairly straightforward to compute the size of the crack tip cavity for a simple 1D ge-
 175 ometry given a specified pressure distribution [e.g. *Fialko and Rubin, 1999*]. However,
 176 this is less obvious when the crack is 2D and pressure boundary conditions are spatially
 177 variable. We developed a method that achieves this for arbitrary dike pressure and ge-
 178 ometry. The process is iterative and is loosely based on simulating the fracture process
 179 during an intrusion. One starts by setting up a grid of dislocation elements that cover
 180 the dike surface. The iterative approach can then be described in the following steps:

- 181 1. Select dislocations elements where magma is located and the dike walls subject
 182 to positive overpressure. This represents the initial singular crack.
- 183 2. Use the boundary element approach (described below) to solve for the dike open-
 184 ing.
- 185 3. Compute normal tractions on the rest of the grid due to both dike opening and
 186 the resolved background stress.
- 187 4. Find elements subject to less compression than the predefined crack under-pressure
 188 at that location. If there are no such elements the stress singularity has been can-
 189 celed to the resolution of the grid, otherwise continue to the next step.
- 190 5. Assign the specified under-pressure to these elements and move to step 2.

191 The vertical distribution of overpressure is parameterized by a single value of magma
 192 pressure at the level of neutral buoyancy $P(z_{LNB})$, where the crustal density is the same
 193 as the magma density. The dike overpressure $\Delta P(z)$ along a vertical cross-section is

$$\Delta P(z) = \rho_m g(z - z_{LNB}) + P(z_{LNB}) - \sigma(z), \quad (1)$$

194 where z is depth, ρ_m is magma density, $\sigma = \sigma_{ij}^T \nu_i \nu_j + P_{litho}(z)$ is the dike normal trac-
 195 tion (ν_i is the dike plane normal vector; thus $\sigma_n = \sigma_{ij}^T \nu_i \nu_j$) due to the stress tensor σ_{ij}^T
 196 derived from tectonic loading and P_{litho} , the lithostatic pressure. The latter is computed
 197 from the density of the Icelandic crust from *Guðmundsson and Högnadóttir* [2007], based
 198 on data from *Carlson and Herrick* [1990] and *Christensen and Wilkens* [1982]. The tec-
 199 tonic stress is computed from a (tapered) buried opening dislocation to model deep rift-
 200 ing and plate spreading. The opening is tapered using a segment of a fourth order poly-
 201 nomial with zero slopes at both ends to attain non-singular stresses (see section 3.1.1 for
 202 details).

203 The lateral extent of dike overpressure is indicated by the parameter L that con-
 204 trols the dike length along strike. We assume that between 0 and L that $P(z_{LNB})$ is spa-
 205 tially constant at any given time. Crack opening beyond L is found by computing the
 206 size of the dike tip cavity that cancels the stress singularity. The initial crack for the al-
 207 gorithm, described above, is taken as the region where $\Delta P > 0$ for all dislocations within
 208 distance L along the dike plane. Thus, L does not represent the fracture length, which
 209 varies with depth, but the length where $\Delta P > 0$ at $z = z_{LNB}$.

210 2.2 Boundary element implementation

211 The surface in which the dike can propagate is fixed based on seismicity and has
 212 fixed dislocation element discretization. This is different from the approach of *Segall et al.*
 213 [2013], where the discretization of the dike evolved as the dike propagated. The latter
 214 approach allows the dike length $L(t)$ to be a continuous variable. In contrast, the ap-
 215 proach here renders $L(t)$ discrete, for computational efficiency admissible lengths are pre-
 216 defined by the initial discretization of the dike. This, in turn, results in an objective func-
 217 tion that is a discrete function of L , precluding gradient-based optimization methods.
 218 In spite of this, there are significant advantages in terms of computational efficiency since
 219 repeated calculations of the Green’s functions are avoided.

220 Consider the matrix of influence coefficients \mathbf{G} that relates a vector of opening \mathbf{b}
 221 to the vector of over-pressure acting on each dislocation element $\Delta\mathbf{P}$ in an elastic half-
 222 space:

$$\Delta\mathbf{P} = \mathbf{G}\mathbf{b} \Rightarrow \mathbf{b} = \mathbf{G}^{-1}\Delta\mathbf{P}. \quad (2)$$

223 Computing \mathbf{G} is computationally expensive. For n opening mode dislocations, \mathbf{G} has n^2
 224 elements. If the crack geometry changes then all or a part of \mathbf{G} changes, such that in
 225 a time-dependent inversion \mathbf{G} typically changes in every iteration. That is the approach
 226 taken by *Segall et al.* [2013], however since they assumed a planar dike, they could use
 227 translational symmetry to reduce the number of function calls. The 2014 Bárðarbunga
 228 dike is not planar, which means that such symmetries do not exist. We, therefore, com-
 229 pute \mathbf{G} only once for a fixed grid and store the matrix. The algorithm outlined in Sec-
 230 tion 2.1 is then used to select dislocation elements that contribute to the opening of the
 231 dike. The rows and columns of \mathbf{G} corresponding to elements outside the periphery of the
 232 dike, including the tip cavity, are removed before the matrix is inverted to solve for the
 233 vector of opening \mathbf{b} .

234 *Ruch et al.* [2016] showed that a small amount of strike-slip was occurred on faults
 235 parallel to the dike and other deformation studies have also suggested that some slip oc-
 236 curred on the dike plane [*Sigmundsson et al.*, 2015; *Spaans and Hooper*, 2018]. Here we
 237 neglect this for two reasons. Firstly, the dominant displacement across the dike is open-
 238 ing, thus the contribution from strike-slip displacements to the deformation and stresses
 239 will be secondary. Secondly, including a strike-slip contribution in \mathbf{G} renders the matrix

240 four times as large. This poses computational problems since the matrix is already very
 241 large and non-sparse.

242 2.3 Modeling the seismicity rate

243 Due to the kinked path of the Bárðarbunga dike, we cannot use the same approach
 244 as *Segall et al.* [2013] where the seismicity rate is computed in rectangular voxels. In or-
 245 der to best utilize the seismicity data, we form a mesh of tetrahedra elements surround-
 246 ing the dike (Figure 4). The tetrahedral mesh is chosen such that voxels do not cross the
 247 dike plane. Dislocations have stress singularities that are proportional to the opening,
 248 or if dislocations align in the same plane, to the difference in opening of two adjacent
 249 dislocations. Thus, a smoothly varying opening will greatly decrease the influence of these
 250 singularities. However, if the voxels intersect the dike plane stresses may be evaluated
 251 too close to a dislocation edge producing un-realistic values. We evaluate the stress ten-
 252 sor at Gauss points in each tetrahedron. Gaussian quadrature only uses points in the
 253 interior of the integration domain, this further limits the influence of singular stresses.
 254 An efficient way to mesh and guarantee that voxels do not cross the dike plane is to use
 255 Delaunay triangulation. It has the property that nearest neighbor points form an edge
 256 of the same triangle. Thus, by making sure any point on the dike plane also has the near-
 257 est neighbor on the dike plane, then the voxels will not intersect the plane of the dike
 258 (Figure 4). The stress tensor evaluated at Gauss-points is then projected into normal
 259 and shear tractions acting on fault planes consistent with observed focal mechanisms.

260 We compute the cumulative number of earthquakes N using the modified Dieterich
 261 1994 theory of *Heimisson and Segall* [2018]:

$$262 \frac{N}{r} = \frac{A\sigma_0}{\dot{s}_b} \log \left(\frac{\dot{s}_b}{A\sigma_0} \int_0^t K(t') dt' + 1 \right), \quad (3)$$

263 where r is the background rate of seismicity for a population, which we define for each
 264 voxel. A is a constitutive parameter related to the direct effect in the rate-and-state fric-
 265 tion law and relates changes in slip rate to friction. τ_0 and σ_0 are the initial shear and
 266 normal stresses acting on the fault and \dot{s}_b is the background Coulomb stressing rate where
 267 the coefficient of friction is $\mu = \tau_0/\sigma_0 - \alpha$. Here, α is a constant relating changes in
 268 normal stress to changes in state [*Linker and Dieterich, 1992*]. The characteristic decay

269 time of seismicity is $t_a = A\sigma_0/\dot{s}_b$. Time dependent stress changes due to the intrusion
 270 are accounted for in the kernel $K(t)$:

$$271 \quad K(t) = \exp\left(\frac{\tau(t)}{A\sigma(t)} - \frac{\tau_0}{A\sigma_0}\right) \left(\frac{\sigma(t)}{\sigma_0}\right)^{\alpha/A}, \quad (4)$$

272 where $\tau(t)$ and $\sigma(t)$ are the total shear and effective normal stress acting on the fault
 273 planes respectively.

274 We apply the trapezoidal rule to the integral (3) in each voxel to estimate the scaled
 275 cumulative number of earthquakes $\tilde{N} = N/r$ at time t_i (where $t_1 = 0$). In the m -th
 276 Gauss point in the n -th voxel the approximation of Equation (3) is:

$$\tilde{N}^{n,m}(t_i) = \frac{A^n \sigma_0^{n,m}}{\dot{s}_b^{n,m}} \log \left(\frac{\dot{s}_b^{n,m}}{A^n \sigma_0^{n,m}} \sum_{j=1}^{j=i} \frac{1}{2} (K^{n,m}(t_j) + K^{n,m}(t_{j+1})) (t_{j+1} - t_j) + 1 \right), \quad (5)$$

277 where $\dot{s}_b^{n,m} = \dot{\tau}_b^{n,m} - (\tau_0^{n,m}/\sigma_0^{n,m} - \alpha^n) \dot{\sigma}_b^{n,m}$ is the background Coulomb stressing rate
 278 at Gauss point m in voxel n . The kernel can be written in the same notation

$$K^{n,m}(t_j) = \exp\left(\frac{\tau^{n,m}(t_j)}{A^n \sigma^{n,m}(t_j)} - \frac{\tau^{n,m}(t_1)}{A^n \sigma^{n,m}(t_1)}\right) \left(\frac{\sigma(t)^{n,m}}{\sigma(t_1)^{n,m}}\right)^{\alpha^n/A^n}. \quad (6)$$

279 For further discussion on the meaning of various parameters and the derivation of equa-
 280 tions (3) and (4) we refer the reader to *Heimisson and Segall [2018]*.

281 We estimate the total number of predicted events in the n -th voxel N^n based on
 282 the scaled number events at the m Gauss points:

$$\tilde{N}^n(t_i) = r^n \frac{\sum_m w_{(n,m)} \tilde{N}^{(n,m)}(t_i)}{\sum_m w_{(n,m)}}, \quad (7)$$

283 where $w_{(n,m)}$ are the Gauss weights of point m in voxel n and r^n is the background rate
 284 of seismicity per unit volume of the n -th voxel.

285 Equation 4 depends on the absolute shear and normal stress acting on a fault plane.
 286 The initial shear stress τ_0 is the component of the traction vector for a given fault ori-
 287 entation parallel to the slip vector and computed directly from the dislocation model of
 288 the plate boundary, discussed in section 3.1.1, and $\Delta\tau(t)$ is the stress change due to dike
 289 opening. These two form the total shear stress: $\tau(t) = \tau_0 + \Delta\tau(t)$.

290 The effective normal stress acting on a population of seismic sources $\sigma(t)$ is a com-
 291 bination of several factors,

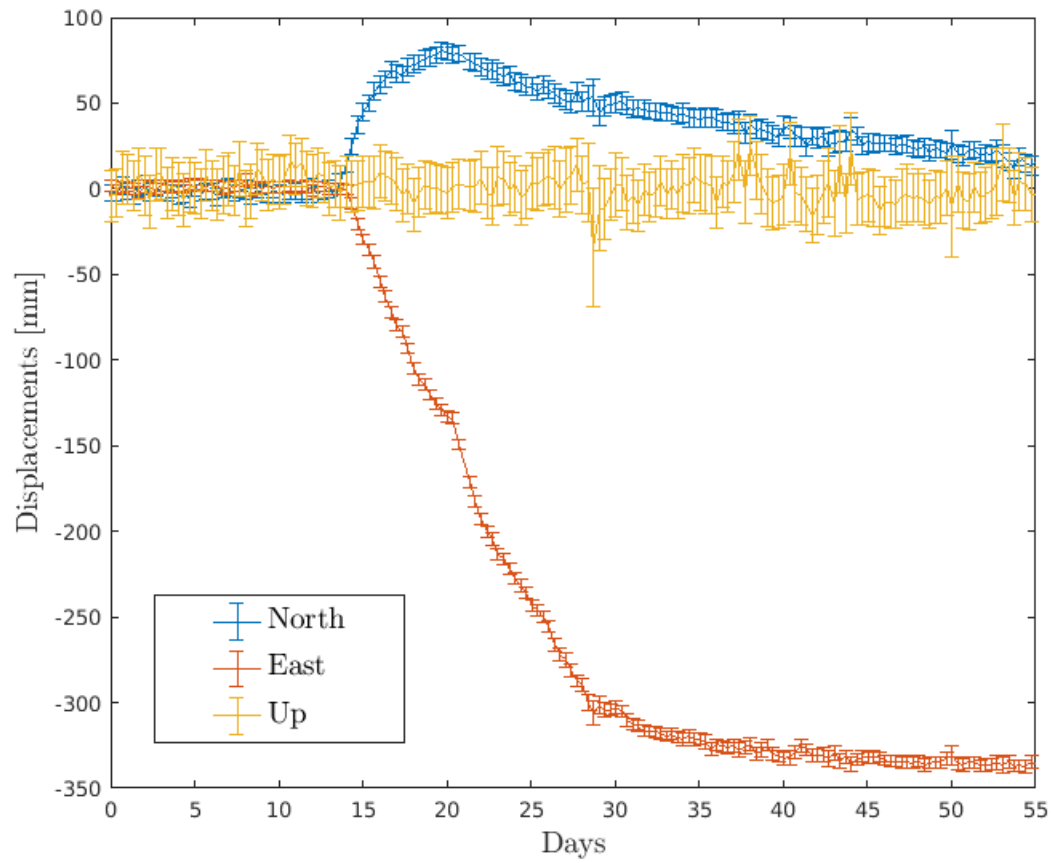
$$\sigma(t) = \sigma_0 + \Delta\sigma(t), \text{ where } \sigma_0 = P_{litho} - \rho_w g z + \sigma_n \quad (8)$$

292 where P_{litho} is the lithostatic pressure estimated from the density structure in Iceland
 293 [*Guðmundsson and Högnadóttir, 2007*], $\rho_w = 1000 \text{ kg/m}^3$ is the density of water and
 294 z the depth below the Earth's surface. σ_n is the normal component of the traction act-
 295 ing on the fault plane due to plate spreading and $\Delta\sigma(t)$ is the time-dependent normal
 296 stress induced by the dike opening. In this paper we use the same notation for stresses
 297 acting on the dike plane and the fault planes, for example, $\sigma(t)$ in both cases reflects the
 298 total normal stress. This is done to emphasize that the dike and faults as subject to the
 299 ambient stress field and are physically consistent.

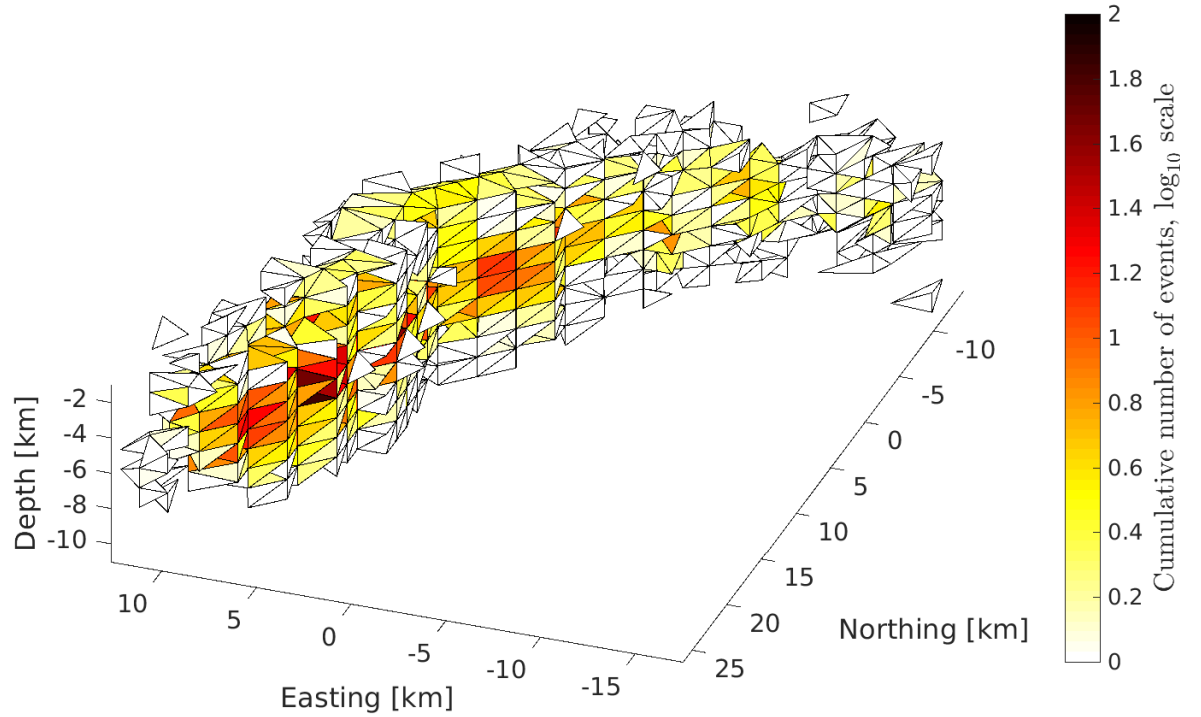
300 2.4 Treatment of observations

301 To determine the cumulative number of events, we first assign each earthquake to
 302 a voxel. We use the catalog of *Ágústsdóttir et al. [2019]* and magnitude estimates from
 303 *Greenfield et al. [2018]* and filter the catalog for the estimated magnitude of complete-
 304 ness of $M_c = 1$. Events not inside any voxel (about 2%) are excluded. The total time
 305 history $N(t)$ is interpolated using a piecewise cubic Hermite interpolating polynomial;
 306 then the interpolant is evaluated at predefined time steps. This interpolation scheme is
 307 shape preserving with continuous first derivative, which guarantees a non-negative seis-
 308 micity rate. To account for hypocentral errors, event locations are randomly perturbed
 309 within the estimated error bounds from *Ágústsdóttir et al. [2019]*. The events are thus
 310 assigned multiple times to voxels; the mean number of earthquakes at time step i in the
 311 n -th voxel is taken to be N_i^n and the standard deviation is σ_i^n , which are used in Sec-
 312 tion 3.3.

313 We estimate that 100 timesteps over a period of 16 days (during which the dike prop-
 314 agated and subsequently erupted) are needed to resolve first order time-dependent fea-
 315 tures in the seismicity. To determine the cumulative GPS displacements at these 100 time
 316 steps we interpolate the 8h time series (Figure 3) using a piecewise linear interpolation.
 317 The interpolation corresponds to upsampling the GPS time series by approximately a
 318 factor of two.



319 **Figure 3.** 8 hour time-series at station DYNC shown as days since August 1 2014. Dike starts
320 propagating at around day 15. Location of DYNC is shown in Figure 1.



335 **Figure 4.** Total number of earthquakes in each voxel, binned into a mesh of voxels with mean
 336 edge length of 1.5 km.

321 **3 Inversion**

322 The model of the dike opening developed in section 2.1 is a function of the tectonic
 323 stress field, the lithostatic pressure gradient, the excess magma pressure and the magma
 324 density itself. All these fields influence the traction boundary conditions on the dike sur-
 325 face. We constrain parameters that control these fields with deformation data (Section
 326 3.1), this will be referred to as the *stress model*. Since these stresses do not change with
 327 time (except the magma pressure) we use InSAR and GPS data spanning the full intru-
 328 sion [data from *Sigmundsson et al.*, 2015] to estimate the time-independent fields. Next
 329 we estimate the time-depend dike length and pressure using the continuous GPS time
 330 series, the resulting time dependent model of dike opening will be referred to as the *dike*
 331 *model*. Finally, frictional and seismicity rate parameters are estimated from a temporal
 332 inversion of the number of earthquakes, given the dike model, this will be referred to as
 333 the *seismicity model* (Section 3.3). In each step, the results of the previous estimations
 334 are used as constraints so that self-consistency is maintained.

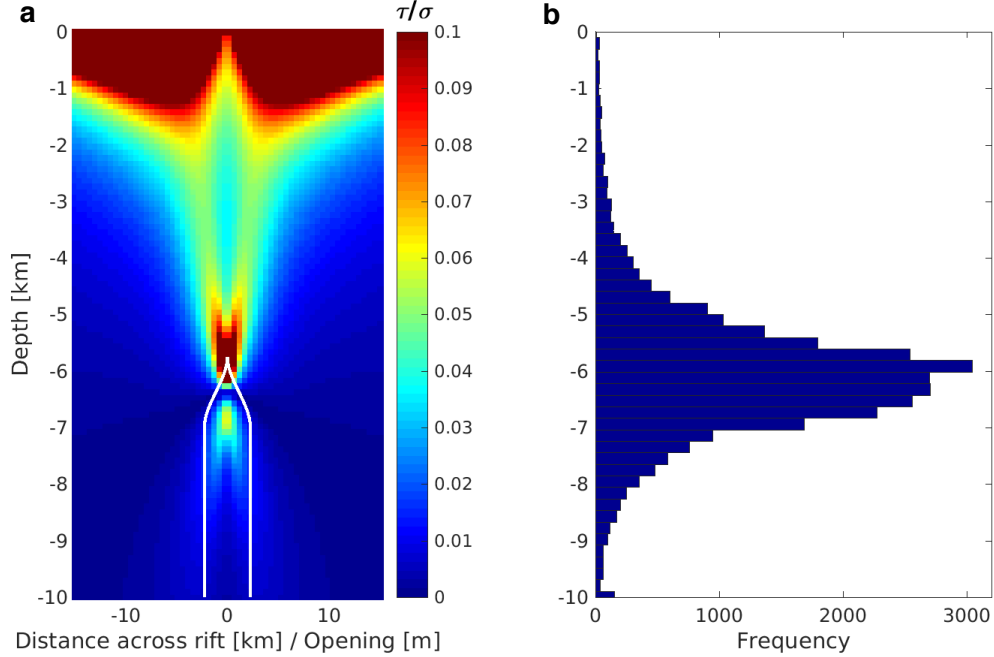
337 **3.1 Constraining the background stress field**

338 **3.1.1 Stress model setup**

339 In this section we describe the stress model and set constraints for optimization based
340 on *a priori* information.

341 Plate boundary deformation in the rift-zones of Iceland has previously been mod-
342 eled using buried dislocations [LaFemina *et al.*, 2005; Árnadóttir *et al.*, 2006]. This as-
343 sumes a constant rate of plate spreading below the brittle-ductile boundary under the
344 central axis of the rift. This is represented as an infinitely deep vertical opening dislo-
345 cation. The buried dislocation model is a highly idealized, yet has been shown to sat-
346 isfy surface deformation data reasonably well in multiple tectonic settings [Savage and
347 Burford, 1973; Hsu *et al.*, 2003; LaFemina *et al.*, 2005; Árnadóttir *et al.*, 2006]. It is thus
348 a reasonable first-order model to capture tectonic stresses that build up between diking
349 events.

350 To eliminate the stress singularity at the edge of the buried dislocation, we taper
351 the opening such that the opening gradient goes to zero at the topmost edge l_u , while
352 at depth l_b the opening reaches the full far-field extension rate. Thus, l_b correspond crudely
353 to the brittle-ductile boundary, where little stress from tectonic loading accumulates (Fig-
354 ure 5). This results in nonsingular stresses at l_b and l_u .



355 **Figure 5.** Depth dependent stress predicted by a tapered buried dislocation. **a** ratio of hor-
 356 izontal shear stress to normal stress assuming lithostatic minus hydrostatic pressure gradient
 357 of $g=1750 \text{ kg/m}^3$ with depth, with shear stress computed on a plane striking 15° east of the rift
 358 axis. Modified buried dislocation opening is shown with white lines with $l_b = 7 \text{ km}$, cumulative
 359 opening of 4.5 m and tapers to 0 at $l_u = 5.75 \text{ km}$ depth. **b** histogram of earthquakes with depth
 360 located by *Ágústsdóttir et al.* [2016]. High ratios of τ/σ promote higher rates of seismicity.

361 In 1797 a dike propagated from Bárðarbunga and erupted in the Holuhraun area.
 362 The 2014 Bárðarbunga dike reoccupied the same crater-row produced in 1797 [*Hartley*
 363 *and Thordarson*, 2013; *Sigmundsson et al.*, 2015]. Over the 217 year time-span between
 364 eruptions, the cumulative opening deficit within the shallow rift zone due to plate mo-
 365 tion is $\sim 4 \text{ m}$, given an extension-rate of 17.4 mm/yr [*Drowin et al.*, 2017]. Extension
 366 over the graben formed by the 2014 Bárðarbunga dike was in fact around 4.5 m [*Ruch*
 367 *et al.*, 2016]. We thus constrain the opening of the buried dislocation to be in the range
 368 $4.0 - 5.0 \text{ m}$. The rift axis strikes $\sim 13.30^\circ - 15.85^\circ$ [*Heimisson et al.*, 2015a], with its
 369 center under the Askja volcanic system north of the 2014 eruption [*Sturkell and Sigmunds-*
 370 *son*, 2000]. The depth to the brittle-ductile boundary is thought to be 6 to 8 km [*Soos-*
 371 *alu et al.*, 2010; *Key et al.*, 2011], based on the depths of earthquakes. However, from
 372 fitting a buried dislocation to the plate boundary deformation in the Eastern Volcanic

373 Zone in Iceland, *LaFemina et al.* [2005] found a best fitting depth of 13 km, although
 374 elastic buried dislocation models ignore possible viscoelastic effects which may bias the
 375 depth. Most earthquakes during the 2014 dike intrusion were between 6 – 8 km depth,
 376 which suggests that 8 km is a lower limit to a range from 8 to 13 km depth for l_b . We
 377 keep the difference $l_b - l_u = 0.5$ km, constant in the inversion described later.

378 The density structure plays an important role in determining the lithostatic stress.
 379 Here, we use estimates from *Guðmundsson and Högnadóttir* [2007] and consider the den-
 380 sity to increase linearly to depth d_t of 4 – 6 km. Below d_t the density is considered con-
 381 stant. We parameterize this density profile through two parameters: $\rho_1 = 2200 - 2400$
 382 kg/m^3 (shallow crust), $\rho_2 = 2850 - 3000 \text{ kg/m}^3$ (density at d_t and below). Typical lab-
 383 oratory measurements of liquid basalt exhibit a range of densities of 2650 – 2800 kg/m^3
 384 [*Sparks et al.*, 1980]. To reflect uncertainty for magma *in situ*, we allow a slightly larger
 385 range of 2600 – 2850 kg/m^3 , so that magma is negatively buoyant in the upper crust.

386 To summarize, we compute the stress before the diking event as a superposition
 387 of a tectonic stress field, derived from a tapered buried dislocation and a density struc-
 388 ture that gives rise to a lithostatic pressure. The buried dislocation model is governed
 389 by the following parameters (see also Table 1): The depth to the top of the dislocation
 390 l_b , its strike and location (± 2.5 km) with respect to Askja caldera center [*Heimisson et al.*,
 391 2015a]). The lithostatic pressure depends on the two densities ρ_1 and ρ_2 and the tran-
 392 sition depth d_t .

394 **3.1.2 Inversion procedure**

395 The previous section described ranges of parameters that determine the remote stress
 396 field. Here we show how these ranges are narrowed to preferred estimates using InSAR
 397 and GPS data. We select 11 interferograms that have been processed and down sampled
 398 by *Sigmundsson et al.* [2015] and GPS displacements from 12 stations (Figure 1) that
 399 span the entire dike intrusion. The dike model is used to predict net GPS displacements
 400 and line of sight displacement for the 11 interferograms. We minimize an L_2 objective
 401 function

$$\chi^2 = (\mathbf{d} - \mathbf{G}_d(\mathbf{m}))^T \boldsymbol{\Sigma}_d^{-1} (\mathbf{d} - \mathbf{G}_d(\mathbf{m})), \quad (9)$$

393

Table 1. Summary of parameters and estimated ranges for the stress model

Symbol	Description	Range	Optimal value
<i>Density structure</i>			
d_t	Depth of density gradient changes	4 – 6 km	4.3 km
ρ_1	Near surface density of the crust	2200 – 2400 kg/m ³	2350 kg/m ³
ρ_2	Density at depth d_t	2850 – 3000 kg/m ³	2900 kg/m ³
ρ_m	Magma density	2600 – 2850kg/m ³	2610 kg/m ³
<i>Buried dislocation</i>			
Strike	Strike (degrees East of North) for rift axis	13.30 – 15.85°	13.30°
l_b	Dislocation locking depth	8 – 13 km	8.0 km
Opening	Net cumulative opening	4 – 5 m	5.0 m
Easting	Uncertainty in Easting location of axis at fixed latitude	±2.5 km	1.36 km

where \mathbf{G}_d represents the forward operator that maps a model parameter vector \mathbf{m} to line of sight surface displacement and east, north, and up GPS components. The corresponding data are contained in vector \mathbf{d} . The variance-covariance matrix, Σ_d , follows *Sigmundsson et al.* [2015] in estimating the spatial covariance of the InSAR data; the GPS error is assumed to be spatially uncorrelated.

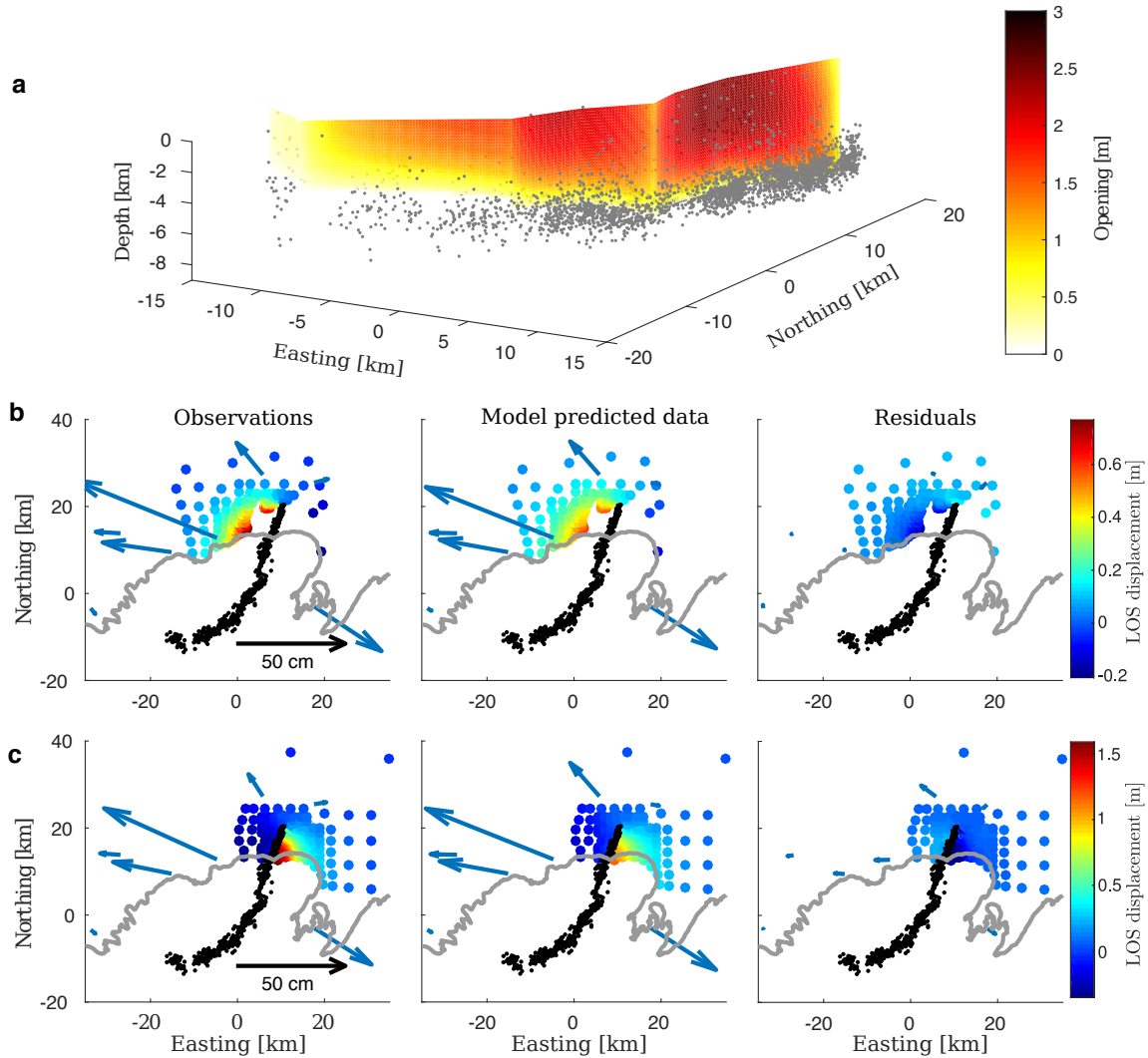
To compute predicted displacements, three parameters are required in addition to those listed in Table 1: ΔV , the volume change of a Mogi source representing caldera deflation at a fixed location [from *Parks et al.*, 2017], $P(z_{LNB})$ from equation 1, and L the dike length. The timespan of the interferograms varies considerably with the later acquisition times ranging from August 26 to September 20, 2014. The length of the dike likely did not change after August 26 [*Sigmundsson et al.*, 2015; *Spaans and Hooper*, 2018], although, the dike pressure and the chamber volume were still evolving. ΔV is inherently time-dependent because the acquisition times of the interferograms are variable. However, at this stage we treat ΔV as constant. Although this does not accurately capture the complicated near-field deformation, which was a combination of a caldera collapse and a deeper depressurization [*Parks et al.*, 2017], it should approximately correct for the far-field displacement from the deeper depressurization.

$P(z_{LNB})$ changes with time and in the next section will be estimated as such. However, in this step of the inversion the goal is to estimate the time-independent parameters and we thus take $P(z_{LNB})$ as constant between August 26 to September 20. Al-

422 though approximating ΔV and $P(z_{LNB})$ as time invariant results in additional misfit
423 between model predictions and data, allowing for different values for every interferogram
424 resulted in a model space that was too large to converge confidently. Most importantly,
425 the values of ΔV , $P(z_{LNB})$ estimated at this initial stage are not utilized in the subse-
426 quent time-dependent inversion.

427 The inversion procedure starts by finding a good fit to the data using a genetic al-
428 gorithm [*Goldberg and Holland*, 1988]; it then attempts to improve the fit further using
429 a direct search algorithm [*Audet and Dennis Jr*, 2002]. Both steps enforce strict bounds
430 on the parameter values (Table 1). Running this scheme repeatedly consistently converges
431 to the same minimum, which we interpret as the global minimum. The optimal values
432 for the stress model are reported in Table 1. These maximum likelihood values are used
433 in the following, time-dependent inversion.

434

3.1.3 Results: Stress model

435 **Figure 6.** The static dike model (a) and comparison of the observations, model predicted data
 436 and residuals for TerraSAR-X (26 July 2012 – 4 Sept. 2014, ascending) (b) and Cosmo-SkyMed
 437 (August 13–29 2014, descending) interferograms (c). Arrows indicate horizontal GPS displace-
 438 ments at the time of the final InSAR acquisition. The bottom edge of the model dike is roughly
 439 coincident with the seismicity.

440 Figure 6 shows the opening distribution of the final dike model and two examples
 441 of interferograms used in the inversion. The lower tapered edge of the dike agrees well
 442 with the depth of earthquakes. This agreement is not enforced and the model space does

443 allow for dikes that would extend substantially deeper or shallower. The deformation resid-
 444 uals indicate good agreement between observations and model predictions.

445 **3.2 Time-dependent estimation of dike pressure and stressing history**

446 In this section, we estimate the dike pressure $P(z_{LNB}, t)$ from continuous GPS data.
 447 As discussed previously, this pressure is assumed constant along the dike length. From
 448 the time-evolution of dike pressure we produce a temporal model of dike opening in space
 449 and time. This model is then used to compute the stressing history in each voxel as func-
 450 tions of time during the intrusion.

451 The 8 hour GPS time series is interpolated into 100 time steps, corresponding roughly
 452 to 1 point per 4 hours. This upsampling was necessary to resolve characteristics of the
 453 seismicity that occur on time scales shorter than 8 hours in Section 3.3. For each time
 454 step the length of the dike $L(t)$ is determined by the advancing seismic swarm; the magma
 455 is assumed to be 1 km behind the location of the highest seismicity rate during that time
 456 step. $L(t)$ does not change if the point of highest seismicity rate retreated relative to the
 457 previous position. Thus, the dike can only lengthen or stay constant.

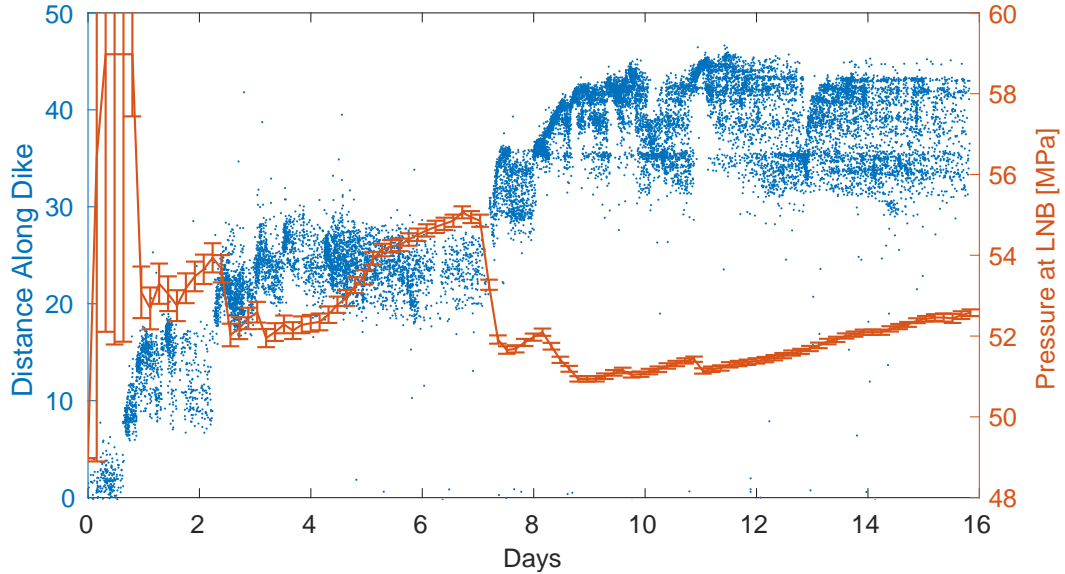
458 At each time step the magma pressure at the level of neutral buoyancy $P(z_{LNB}, t)$
 459 is optimized by fitting the GPS data. An objective function of the same form as equa-
 460 tion 9 is minimized. At the beginning of each time step, we find the least squares solu-
 461 tion for the volume change of a Mogi source, representing the deflating magma reservoir.
 462 Two stations VONC and HAUC (Figure 1) are used to constrain this volume change since
 463 they are close to the caldera and show limited sensitivity to the dike. The predicted dis-
 464 placements from the Mogi source are then used to correct the GPS time series at other
 465 stations before the time-dependent dike inversion is performed. We apply this correc-
 466 tion instead of inverting for $P(z_{LNB}, t)$ and volume change of the Mogi source simulta-
 467 neously due to the computational requirements needed to converge in this time-varying
 468 2D model space. Furthermore, the deflation signal away from the caldera is much less
 469 than the dike signal. Note that because the dike geometry (i.e., which dislocations open)
 470 depends on the pressure $P(z_{LNB}, t)$, this step is a non-linear inversion.

471 In summary, from the inversion of time-dependent GPS data we obtain $P(z_{LNB}, t)$
 472 while $L(t)$ is determined from the location of the maximum seismicity rate. This, along
 473 with the time-independent parameters (determined in Section 3.1.3) is sufficient to de-

474 rive an opening distribution for the dike at each time step. Using elastic Green's func-
475 tions the dike opening is used to compute the full stress tensor at Gauss points in each
476 voxel surrounding the dike. The time history of the stress tensor at each Gauss point
477 is used in the next step to compute the cumulative number of seismic events and com-
478 pare to observations (Section 3.3).

479 We found that it was not sufficient to represent the stressing history in only 100
480 time steps. We thus assume that between time steps the dike grows at a constant ve-
481 locity and evaluate the stress, at each Gauss point, every 200 m of dike advance. The
482 procedure results in a stressing history of ~ 1000 time steps. We found that the results
483 are insensitive to downsampling the stressing history by 50%, which implies convergence
484 of equation 6. Several tests were made to check errors associated with the calculation
485 of N (equation 7), this included changing the size of the dike elements, and varying the
486 number of Gauss points and voxel size. We found that the current scheme: dislocations
487 with an edge length of 200 m, voxels with a characteristic length of 1500 m and 3 point
488 Gaussian quadrature (27 points in each voxel), resulted in a numerical error much smaller
489 than the data variance.

490

3.2.1 Results

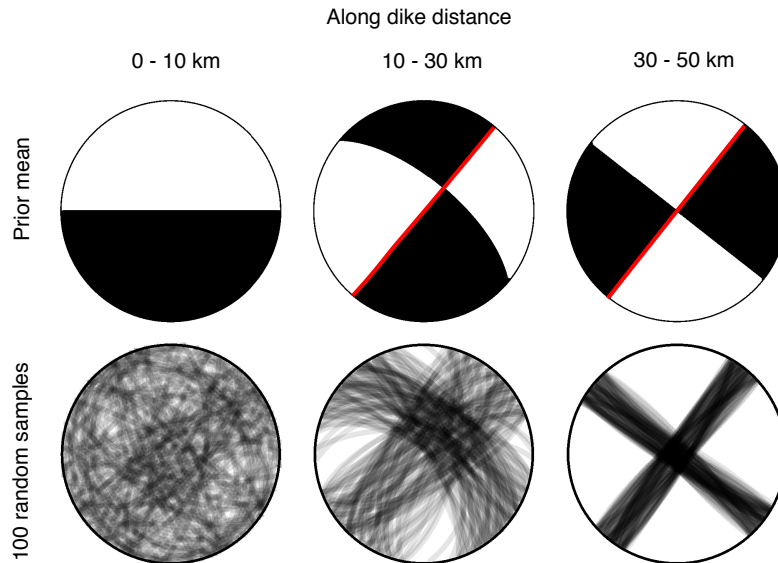
491 **Figure 7.** Comparison of the inferred time-dependent magma pressure at the LNB, based on
 492 inversion of time-dependent GPS data and the space-time evolution of the seismic swarm. Error
 493 bars are one standard deviation. As the dike advances the pressure drops and when arrested the
 494 pressure builds up. The dike model is magmatic and the pressure is assumed constant along
 495 the dike strike at any given time

496 Results for $P(z_{LNB}, t)$ are shown in Figure 7, with an estimate of uncertainty de-
 497 rived by fixing the dike geometry to the optimal value found by the non-linear inversion
 498 scheme in Section 3.2. With fixed dike geometry, the inverse problem is linear, and prop-
 499 agation of uncertainties in the GPS data to errors in the pressure estimate is straight-
 500 forward. This reveals that initially, when the dike is short, the pressure is highly uncer-
 501 tain.

502 Figure 7 shows that the dike pressure increased during pauses in dike advance and
 503 dropped once rapid propagation recommenced, consistent with the interpretation of *Sig-*
 504 *mundsson et al.* [2015]. During the pauses in propagation, inflow of additional magma
 505 continued resulting in increased pressure, but when the dike advanced the pressure de-
 506 creased. These processes are not explicitly prescribed by the dike model but are required
 507 to fit the GPS data. Comparison to Figure 3 reveals that at times when the pressure de-

508 creased, the GPS displacements generally increased. This is simply because far-field dis-
 509 placements are mostly sensitive to the dike volume and the crack surface area increased
 510 during the pressure drops, more than compensating for the pressure reduction. All GPS
 511 stations that recorded the entire event are in the far-field, near field stations like URHC
 512 (Figure 1) were transformed from campaign benchmarks to continuous stations only once
 513 the dike was fully formed. It is worth reiterating that the results in Figure 7 are only
 514 constrained by inverting the continuous GPS, not the seismicity data. The seismicity at
 515 this stage is used only to determine the location of the dike tip.

516 3.3 Seismicity model: Inversion in voxels for seismic source and frictional 517 properties



518 **Figure 8.** Visualization of the prior distributions on focal mechanisms. Top row shows the
 519 focal mechanism corresponding to the mean of the strike, dip and rake priors. Red line indicates
 520 the assumed fault plane. Bottom row shows 100 random samples from the prior distributions.
 521 Columns correspond to distance along dike length: the mechanism is uncertain for range 0 – 10
 522 km, reasonably well constrained for 10 – 30 km and tightly constrained for > 30 km [Ágústsdóttir
 523 *et al.*, 2019].

524 In the previous two steps, we constrained the background stress field and the time-
 525 dependent dike-induced stresses based on geodetic and seismic data. In this section, we

526 use those estimates to predict the cumulative number of earthquakes in each voxel (N
 527 in equation 3). Although many fields and parameters have been constrained in the pre-
 528 vious steps, there are 6 additional parameters that relate to N , three characterizing the
 529 receiver fault orientation: strike, dip and rake, and three related to frictional properties
 530 and background stressing rate: A , α and r . We use a Markov Chain Monte Carlo (MCMC)
 531 approach to estimate posterior probability density functions for fault orientation (strike,
 532 dip, and rake) from focal mechanisms and earthquake production parameters (A , r , and
 533 α). All prior distributions are taken to be uniform with hard bounds, which are described
 534 below.

535 We estimate strike, dip, and rake based on focal mechanisms and inferred fault planes
 536 from *Ágústsdóttir et al.* [2019]. For the first 10 km of the dike, a voxel can have essen-
 537 tially any fault orientation that could be considered reasonable for a rift setting (Fig-
 538 ure 8), this is done to reflect the highly variable and uncertain focal mechanisms in this
 539 area. We allow either strike slip (both left and right lateral), normal or oblique (between
 540 strike slip and normal) with the dip constrained to be between $60 - 90^\circ$. For the distance
 541 range of 10 – 30 km the focal mechanisms exhibit right lateral strike slip with a strike
 542 of $\sim 40^\circ$. However, we allow for uncertainty in dip, strike, and rake (Figure 8) to reflect
 543 the focal mechanism variability. For the final 30 km, the focal mechanisms are tightly
 544 constrained, which translates into low variance in the prior distributions (Figure 8).

545 The prior for the constitutive frictional parameter A is set to a wide range 10^{-5}
 546 to 0.02. The upper limit represents the highest values from lab experiments under el-
 547 evated pore-fluid pressure and temperature [*Blanpied et al.*, 1991]. The lower limit is es-
 548 timated from the values of $A\sigma_0$ that are commonly inferred when the *Dieterich* [1994]
 549 theory is applied to field data [*Hainzl et al.*, 2010]. The parameter α is related to instan-
 550 taneous changes in the frictional state due to changes in normal stress [*Linker and Di-*
 551 *eterich*, 1992]. We set α to a range of 0 – 0.5. We reject seismicity models where τ_0 , μ ,
 552 $\dot{\tau}_b$ or \dot{s}_b are negative, which enforces additional constraints locally on possible fault planes
 553 that are not reflected in Figure 8, and guarantee that only fault orientations are consid-
 554 ered that are subject to stresses favorable for slip.

555 The prior on background seismicity rate ranges from $2 \cdot 10^{-2}$ to 10^{-5} events per
 556 year for a voxel of average size. The seismicity model includes ~ 500 voxels, which means
 557 that at the upper bound we would expect on the order of 10 events per year. Prior to

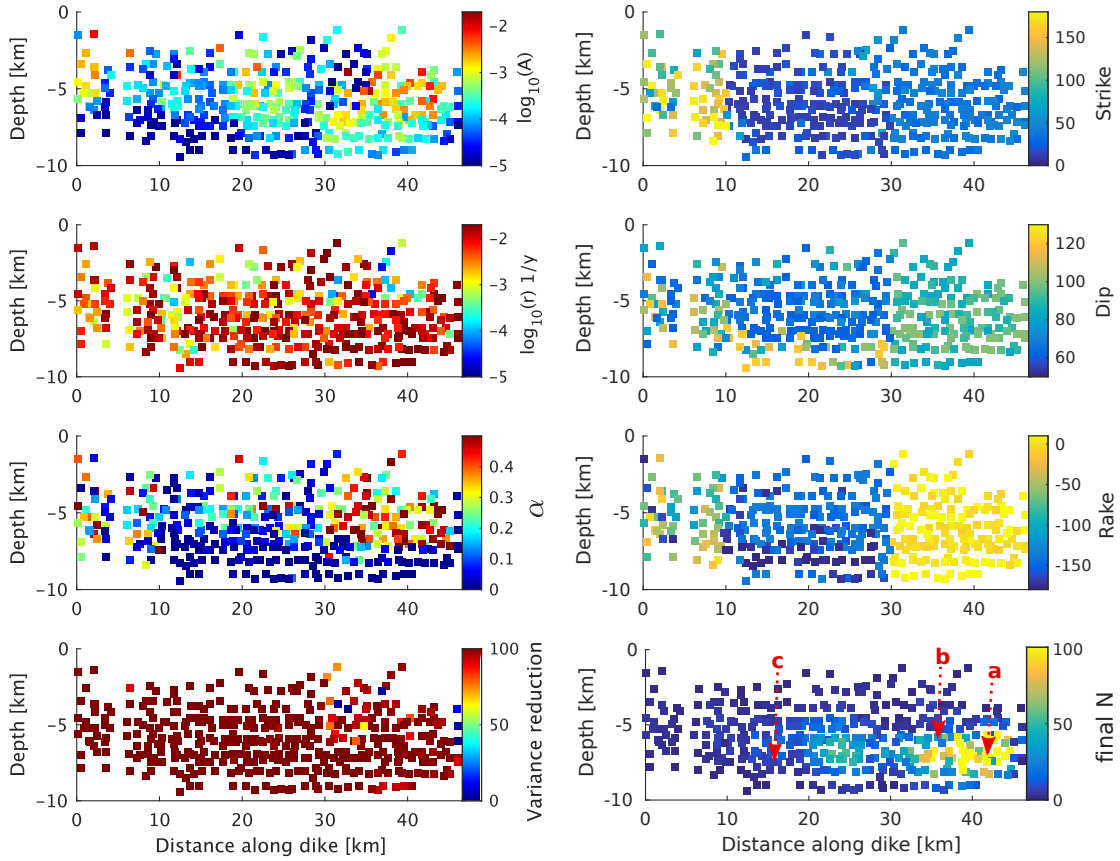
558 the 2014 diking event, no seismicity had been detected on large parts of the eventual dike
 559 path [Ágústsdóttir *et al.*, 2019]. We estimate the magnitude of completeness for the dike-
 560 induced events to be $M_c = 1$, considerably lower than that for the national seismic net-
 561 work. Small background events may, therefore, not have been detected. Nevertheless,
 562 it is likely that 10 events per year would have resulted in some large enough to be de-
 563 tected over the 23 years of seismic monitoring prior to the 2014 Bárðarbunga intrusion.
 564 However, the population of seismic sources (see *Heimisson* [2019] for precise definition)
 565 may not have been sufficiently stressed prior to the intrusion to produce earthquakes at
 566 a constant rate. Indeed, Figure 5 suggests that in most places the background shear to
 567 normal stress ratio was fairly small. In this case, a steady-state background rate would
 568 not have been reached prior to the diking event [*Heimisson and Segall*, 2018] (see sec-
 569 tion 4.1 for further discussion), and could be much higher than what can be inferred from
 570 observations. In this context, the background rate is the steady state seismicity rate that
 571 would eventually occur if the populations of seismic sources were subject to constant back-
 572 ground stressing rate. We thus conclude that a broad *a priori* range is needed to reflect
 573 this uncertainty.

574 Sampling of the PDFs is done using an ensemble sampler algorithm proposed by
 575 *Goodman and Weare* [2010] (using the implementation of *Foreman-Mackey et al.* [2013]).
 576 The algorithm samples the log posterior distribution for the n -th voxel:

$$\log(p(\mathbf{m}^n, \boldsymbol{\sigma}^n | \mathbf{d}^n)) = -\frac{1}{2} \sum_i \left(\frac{N_i^n - \tilde{N}^n(\mathbf{m}^n, t_i)}{\sigma_i^n} \right)^2 - \sum_i \log(\sqrt{2\pi}\sigma_i^n) + \log(p(\mathbf{m}^n)), \quad (10)$$

577 where N_i^n is the cumulative number of seismic events at the i -th timestep and σ_i^n is the
 578 corresponding standard deviation. $\tilde{N}^n(\mathbf{m}^n, t_i)$ represents the forward operator that takes
 579 in the six aforementioned model parameters, \mathbf{m}^n (as well as the pre-computed space-
 580 time variable stress field), and predicts the cumulative number of events in each voxel
 581 from Equation (7). Finally $p(\mathbf{m}^n)$ is the prior probability distribution of the model pa-
 582 rameters in the n -th voxel.

583

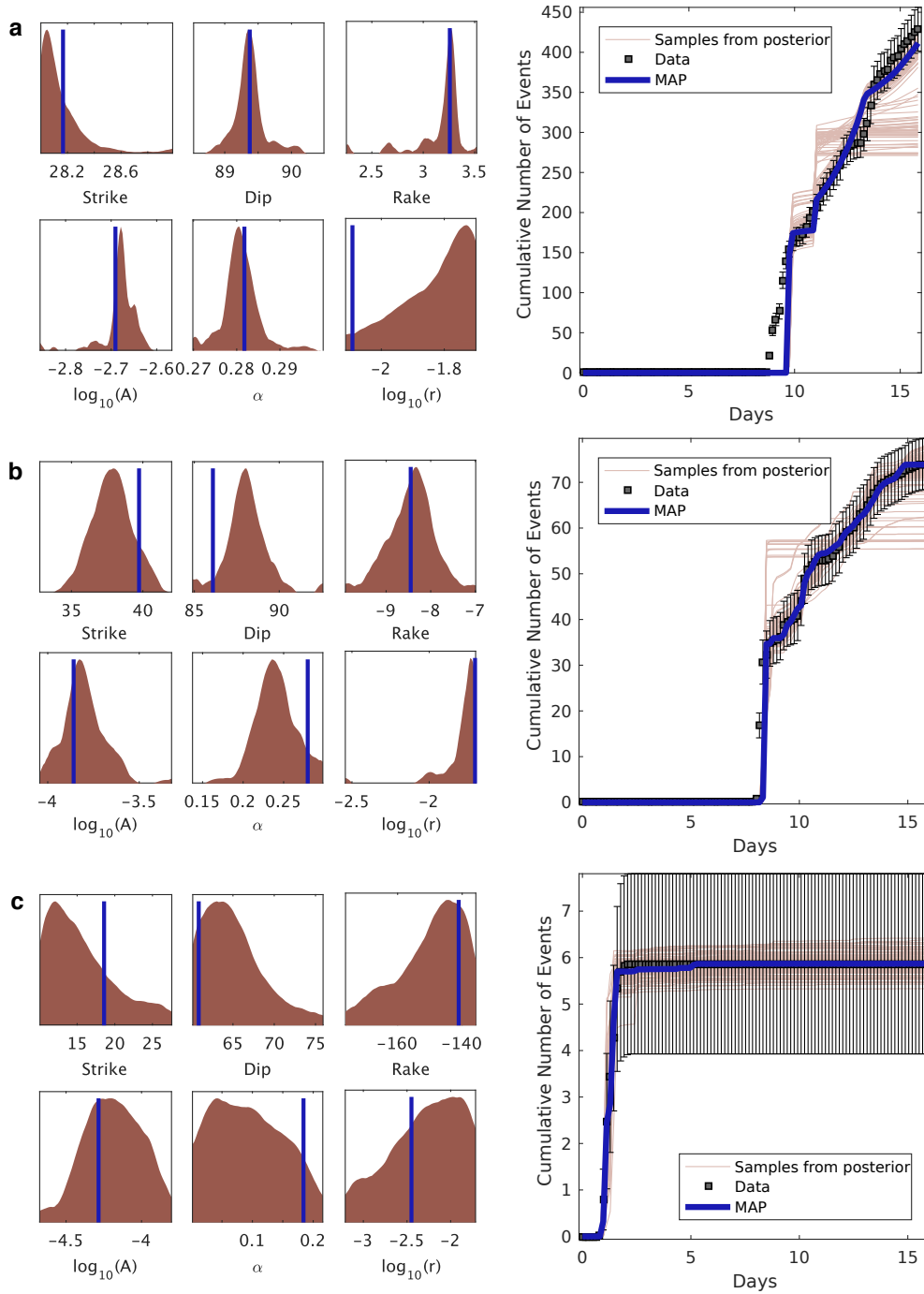
3.3.1 Results: voxel inversion

584 **Figure 9.** Maximum a Posteriori (MAP) values for model parameters estimated in each voxel,
 585 along with variance reduction and final cumulative number of events in the bottom row. Labels
 586 **a**, **b** and **c** and corresponding arrows (bottom right) indicate the locations of voxels shown in
 587 Figure 10. Each square represents the center of a voxel projected in depth versus distance-along-
 588 dike coordinates.

589 Inversion results (Figure 9) exhibit high spatial variability in many parameters of
 590 interest. The MAP (maximum a posteriori) estimate of A ranges from typical laboratory
 591 values ($A \sim 0.01$) to much smaller values ($A \sim 10^{-5}$). The parameter estimates
 592 are spatially correlated, although no such correlation or smoothing is prescribed in the
 593 inversion. This may suggest robustness in the inversion, although, if some models assump-
 594 tions are incorrect, this could systematically bias parameter estimates. One such bias
 595 may stem from the assumed dike tip under-pressure, which was taken to be the end mem-

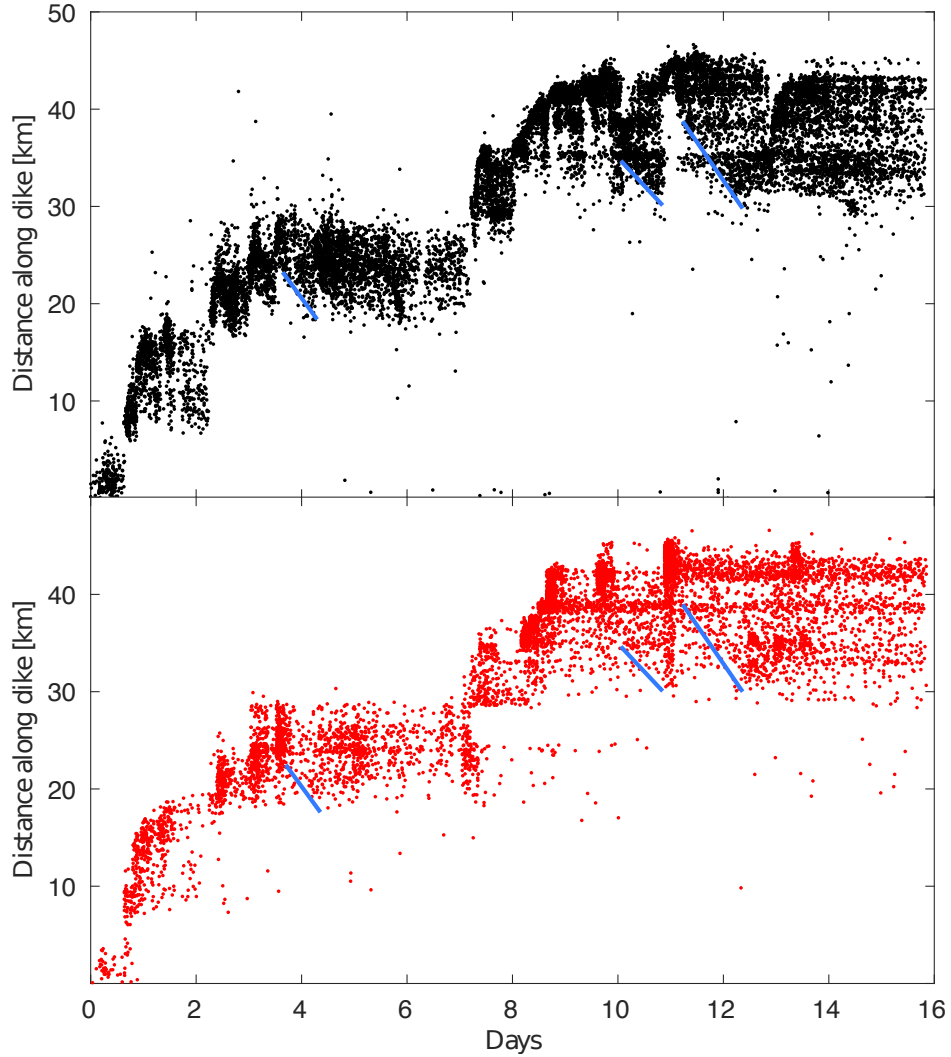
596 ber case of negligible tip pressure ($\Delta P = -\sigma$). With higher dike-tip pressure ($\Delta P =$
597 $P_f - \sigma$), the near field stress perturbations are lower and distributed differently, which
598 may systematically bias A . However, most of the recorded earthquakes are not located
599 at the dike tip, but at the bottom of the dike where the opening tapers due to the ver-
600 tical gradient in overpressure (Figure 6a). Thus, the influence of the leading dike tip on
601 the temporal evolution of the earthquakes may be modest.

602 In the supplementary materials, we show the median value for each distribution,
603 as well as 5% and 95% percentile values (Figures S1, S2, and S3). Figure 9 demonstrates
604 that in the vast majority of voxels, the seismicity model can explain most of the vari-
605 ance in the data. Figure 10 shows the probability distributions for three different vox-
606 els, which vary substantially in temporal behavior and the final cumulative number of
607 events. This figure highlights the influence of the cumulative number of events on the
608 width of the posterior distributions. There tends to be a narrow range of model param-
609 eters that can fit voxels with more than 100 events, whereas voxels with only a hand-
610 ful of events have much broader distributions (see also Supplementary Figures S2 and
611 S3).



612 **Figure 10.** Parameter distributions (left) and predicted/observed cumulative number of
 613 events for three voxels a,b, and c (locations shown in Figure 9, bottom - right), vertical bar
 614 marks the MAP value and distributions are shown over their 95% confidence intervals. Voxels
 615 were picked to illustrate a wide range of cumulative number of events with panel **a** showing the
 616 voxel with the maximum number of events. The range of acceptable models strongly depends on
 617 the cumulative number of events.

618 The fit to the cumulative number of events curves, $N(t)$ is generally good (Figures
619 9 and 10). To further investigate if the seismicity model resolves important space-time
620 characteristics of the seismicity induced by the Bárðarbunga dike, we generate a synthetic
621 catalog. To do so, we round each predicted $N(t)$ time-series from the MAP model to the
622 nearest integer, rendering time-discrete events. We then assign a time to each event by
623 sampling from a uniform distribution with bounds at the previous and subsequent time
624 steps. This procedure reveals that many of the important characteristics of the observed
625 seismicity are reproduced by the model (Figure 11). Most importantly, the seismicity
626 model predicts that actively intruding segments remain seismically active while all pre-
627 vious segments become more or less aseismic. The model generally matches the total num-
628 ber of events in each voxel quite well, as reflected in the variance reduction (Figure 9).
629 For computational reasons, we only run the inversion on roughly half the voxels and, there-
630 fore, do not match the absolute number of events in the catalog. However, the voxels se-
631 lected for MCMC sampling are picked to represent all seismically active regions surround-
632 ing the dike in an unbiased manner. For a 3D view of the dike model and simulated seis-
633 micity see the supplementary movie (Movie S1).



634 **Figure 11.** Comparison of observed and predicted seismicity interpreted in the form of in-
 635 individual events. Black dots show detected earthquakes, red dots are simulated events based on
 636 the MAP model prediction of the cumulative number of events. Blue lines indicates examples of
 637 back-propagation of seismicity and the corresponding locations in the predicted seismicity (see
 638 Section 4.2 for discussion of the back-propagation)

639 4 Discussion

640 4.1 Background seismicity rate

641 One of the most significant uncertainties in this study is the background seismic-
 642 ity rate in each voxel. Very few events had been previously detected in the area where
 643 the dike propagated. Does that mean the background seismicity rate is zero? One pos-

644 sible explanation is that it is very low, with no events large enough to be detected by
 645 the national network. The temporary seismic network in the area during the intrusion
 646 was able to detect much smaller events than the Icelandic permanent seismic network
 647 (SIL network). However, the MCMC sampling suggests that most voxels have a back-
 648 ground seismicity rate near the upper limit, set at one event per 50 years. If that is cor-
 649 rect, it is unlikely that no events would have been detected before 2014. We thus favor
 650 the explanation that seismic sources were not sufficiently stressed to produce earthquakes
 651 prior to the intrusion, but once exposed to the large dike-induced stresses were driven
 652 to failure. We made some attempts at estimating this threshold using a non-constant
 653 background rate model (equations 34 in *Heimisson and Segall* [2018]). However, due to
 654 uncertainty in the dike tip location and the fact that the two predictions are equivalent
 655 once the threshold is reached, these attempts did not give meaningful results and gen-
 656 erally predicted a negligible threshold. In contrast, if we had placed the dike tip slightly
 657 ahead of the swarm, then such a threshold would be required. We conclude that the dike
 658 and post rifting period release most of the inter-diking stresses leaving the crust in a low-
 659 stress state. Indeed, previous studies found the dike opening agreed well with the expected
 660 strain accumulation since the last intrusion [*Ruch et al.*, 2016]. The absence of background
 661 seismicity prior to the diking event does not negate the use of the modified Dieterich the-
 662 ory, provided that the stress changes due to the dike are sufficient to elevate the pop-
 663 ulation well above steady state friction [*Heimisson and Segall*, 2018].

664 4.2 Segmentation of seismicity and back-propagation

665 The seismicity model reproduces the segmentation of the seismicity along the dike,
 666 where the newest segment remains seismically active until the next segment is formed.
 667 Once the formation of a new segment is underway very few earthquakes occur in the pre-
 668 vious segments (Figure 11). This behavior can be physically understood from Figure 7,
 669 where in general the pressure drops as the dike grows, although it increases transiently
 670 when the dike stalls. During a pause, the seismic sources are exposed to increasing stresses
 671 as the pressure recovers. The seismicity rate R depends on the integral of the stress ker-
 672 nel $K(t)$ (equation 4):

$$673 \frac{R}{r} = \frac{K(t)}{1 + \frac{s_b}{A\sigma_0} \int_0^t K(t') dt'}, \quad (11)$$

674 which means that during the pauses the integral in the denominator increases and, in
 675 physical terms, the population develops a stress memory or threshold, and will not be

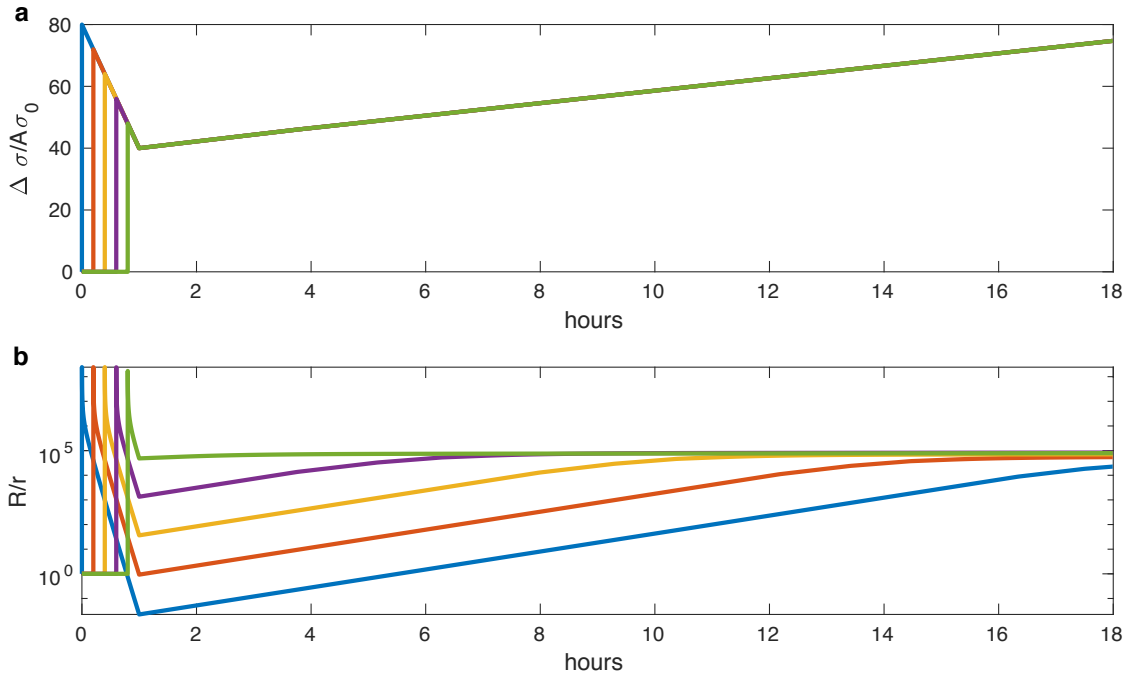
676 significantly activated again unless the stress change exceeds the previous peak. In sum-
 677 mary, as a segment of the dike intrudes, the pressure increases and reaches a maximum
 678 before the next segment is formed. Because the pressure never sufficiently exceeds the
 679 previous maximum, the previous segments are not reactivated seismically. Such a stress
 680 memory (Kaiser-effect) has been previously identified in triggering of volcano-tectonic
 681 earthquakes [Heimisson *et al.*, 2015b].

682 In some parts of the dike, where abrupt changes in direction (or kinks) occur, there
 683 is also a significant stress rotation that affects source populations near the kink. For ex-
 684 ample, a very clear shutoff of seismicity occurs in the simulated catalog (Figure 11) around
 685 day 7.5 and distance 25–29 km. This abrupt shutoff is due to the geometry of the kink,
 686 which causes a stress shadow. However, in most other parts of the dike, the segmenta-
 687 tion in seismicity is caused by the stress memory effect. Magma solidification in the nar-
 688 rower lower and/or upper reaches of the dike may also play a role, by changing the com-
 689 pliance of the dike, and by altering the location of the largest induced stresses. However,
 690 solidification is not included in our model and is thus not needed to explain the large scale
 691 segmentation of the seismicity.

692 Another striking feature of the seismicity is several occurrences of backward prop-
 693 agation at an approximately constant speed. Three of these are marked in Figure 11. The
 694 simulated catalog shows some evidence for back-propagations at these times, however
 695 this is not as clear as it is in the observed seismicity. The difference between model and
 696 observations may be in part due to discretization in space and time, which limit the res-
 697 olution of the simulated catalog. Alternatively, the back-propagation could be due to physics
 698 which are not modeled in this study.

699 We suggest that back propagation may also be explained by stress memory effects,
 700 as follows. When the dike advances the pressure drops, from Figure 7 we estimate that
 701 the pressure drop is about ~ 2 MPa/h. The stress sensed by the populations of seismic
 702 sources drops approximately proportionally. Once the dike halts it begins re-pressurizing
 703 (at a rate of about ~ 0.1 MPa/h). Thus, seismic sources along the length of the dike
 704 that have experienced different peak stresses, with more distal sites experiencing lower
 705 peak stress, will reactivate at different times. To test this hypothesis, we compute the
 706 seismicity rate for hypothetical populations that have been exposed to varying peak stress
 707 that decreases with dike propagation distance. Once a minimum stress is reached, all pop-

708 ulations are subject to the same slow re-pressurization (Figure 12). Due to the stress mem-
 709 ory effect, the populations are reactivated at different times and together produce back-
 710 propagation of seismicity at a constant speed that is proportional to the re-pressurization
 711 rate. Further study of the back-propagation is needed, in particular, to exclude other po-
 712 tential explanations and to explore more direct comparison with data at finer spatial res-
 713 olution.



714 **Figure 12.** Idealized stressing histories that produce back-propagation of seismicity at
 715 roughly constant speed. **a** stress history at different points adjacent to the dike; **b** corresponding
 716 seismicity rate. As the dike advances the pressure decreases and the peak stress sensed by seismic
 717 sources decreases with propagation distance (blue to green lines). Once the dike propagation
 718 halts, a slow re-pressurization begins, which is approximately the same for all source populations.
 719 Each population of sources is only significantly reactivated once the stress reaches the previous
 720 peak value.

721 It is generally agreed that the propagation of dike-induced seismic swarms result
 722 directly from the propagation of the dike. We further suggest that many spatiotempo-
 723 ral complexities in the dike induced seismicity result largely from the interplay of time-
 724 dependent pressure and stress memory effects. As a consequence the turning on and off

725 of seismicity may indicate transient pressure changes, where seismicity rate increase rapidly
 726 upon exceeding previous pressure levels. In summary, the seismicity does not directly
 727 measure the current state of stress at a point in the crust but rather responds to the re-
 728 cent stressing history of that point. Additional information from geodetic measurements
 729 is, therefore, essential to deconvolve the stressing history and the observable seismicity.

730 4.3 Secondary triggering

731 Where the *Dieterich* [1994] theory has been used in a similar manner as in this study,
 732 it has been noted that there may be biases due to source interactions and secondary events
 733 [Segall *et al.*, 2013; Inbal *et al.*, 2017], effects that are not included in the theory. Sev-
 734 eral algorithms have been developed to decluster earthquakes and remove aftershocks
 735 or secondary events, but each method is based on different assumptions and generally
 736 produce different results when applied to the same catalog [Marsan and Lengline, 2008].
 737 Moreover, most declustering methods are made to separate mainshocks from aftershocks.
 738 Dike intrusions are striking examples of extremely strong spatial and temporal cluster-
 739 ing not primarily driven by mainshock - aftershock triggering, but by the time evolution
 740 of the stress field induced by the dike. Thus, it can be argued that most declustering meth-
 741 ods are not appropriate for such a sequence.

742 Furthermore, *Heimisson* [2019] challenged the view that declustering is required
 743 when applying the Dieterich theory. He showed, under a few assumptions that hold fairly
 744 generally, that populations of seismic sources with and without interactions produce the
 745 same seismicity rate when perturbed, if they have the same background seismicity rate.
 746 This indicates that a population with interactions can be approximated as a population
 747 without interactions with the same long term average background seismicity rate. In ad-
 748 dition, *Heimisson* [2019] showed that interaction between populations in a spatially het-
 749 erogeneous stress field, do not change the absolute number of events on a regional scale
 750 for times $t \gg t_a$. This suggests that interactions do not change the absolute number
 751 of events, although they may somewhat change their temporal and spatial distribution.
 752 These results indicate that the assumption of non-interacting sources may not be as con-
 753 sequential as it seems. Given this, we suggest that using the full seismic catalog intro-
 754 duces less bias than declustering, which may likely remove physically relevant spatial and
 755 temporal correlations in the seismicity.

756 4.4 Validation of *Dieterich* [1994]

757 Our results support the applicability of the *Dieterich* [1994] theory to temporally
 758 complicated and large magnitude stress changes. The results show that the theory is con-
 759 sistent with the cumulative number of events in most voxels even after independent ob-
 760 servations such as GPS and InSAR have been used to constrain the complete stressing
 761 history in each voxel. In that sense, the results provide significant observational valida-
 762 tion of the theory since the temporal evolution of the cumulative number of events is strongly
 763 controlled by stressing history. However, in order to match the observations, it is nec-
 764 essary to constrain time-independent parameters in each voxel, and some of those pa-
 765 rameters must be spatially heterogeneous (Figure 9).

766 4.5 Further development of joint inversions for dike propagation

767 *Segall et al.* [2013] proposed imaging a propagating dike through simultaneous joint
 768 inversion of both earthquakes and deformation, where deformation is sensitive to the in-
 769 flation of the dike, but earthquakes better constrain the location of the dike tip. They
 770 tested the method on the Father’s day dike intrusion on Kilauea, that had about 200 recorded
 771 earthquakes, and simultaneously fit the cumulative number of events and GPS time-series
 772 assuming spatially uniform background stresses and frictional parameters. This study
 773 demonstrates, however, that voxels with few events can be fit with a wide range of pa-
 774 rameters, but when the number of events exceeds about one hundred, the fit can be achieved
 775 only within a very narrow range of parameters. Performing such joint inversion for the
 776 2014 Bárðarbunga dike would require accounting for spatially variable frictional prop-
 777 erties, initial stress, or short wavelength features in the dike-induced stress in some stochas-
 778 tic manner, since uniform frictional properties are not consistent with the observations.

779 Additional improvements in the joint inversion strategy might involve estimating
 780 the receiver fault orientation directly based on the observed seismicity and a model of
 781 the dike-induced stress changes. We made some attempts to constrain the activated fault
 782 planes based on the dike model and time history of seismicity in each voxel. Preliminary
 783 results suggested that sometimes the correct fault plane was recovered, however frequently
 784 the inversion converged to other fault planes that fit the data equally well, or better. While
 785 the preliminary results were promising, we concluded that this was beyond the scope of

786 the study and instead constrained the fault planes to be consistent with the observed
787 focal mechanisms.

788 Looking ahead, one goal of joint inversions of seismic and geodetic data to image
789 a dike would be to do so in real-time. This task involves further challenges, in partic-
790 ular, related to the lack of prior knowledge of the dike path. In some places, dikes prop-
791 agate along a rift zone, such that the path may be known reasonably beforehand, but
792 because voxels should not intersect the dike plane that knowledge of the trajectory would
793 need to be precise. In the more general case, the problem will require adaptive mesh-
794 ing that can follow the dike as it propagates.

795 5 Conclusions

796 We have developed methodology for analyzing deformation and seismicity together
797 with a single physics-based dike model. The approach makes use of geodetic data (In-
798 SAR and GPS) and seismic data (earthquake locations and focal mechanisms) to con-
799 struct a dike model that predicts both deformation and seismicity. The model was ap-
800 plied to the spatially and temporally complex 2014 Bárðarbunga diking event. The re-
801 sults shed light on the physics of dike-induced earthquakes, which are found to be con-
802 sistent with elastic stress transfer onto preexisting faults, as previously suggested [e.g.
803 *Rubin and Gillard, 1998*].

804 We applied the modified Dieterich theory [*Heimisson and Segall, 2018*] to a more
805 complicated stressing history than previous studies. The inversion of the cumulative num-
806 ber of earthquakes provides a rare insight into the frictional properties of the crust. We
807 find that the constitutive parameters A and α exhibit considerable variability, but are
808 spatially correlated. The correlation is not imposed through spatial smoothing and may
809 suggest robustness of the inversion process and methodology.

810 The GPS inversion indicates that on average magma pressure drops when the dike
811 propagates, and recovers when the dike stalls. This may explain the characteristic seg-
812 mentation of the Bárðarbunga dike as a manifestation of a stress threshold or memory
813 effect, because the stress never becomes sufficiently large to reactivate the previous seg-
814 ments.

815 Acknowledgments

816 We thank Tim Greenfield, Bob White and Thorbjörg Ágústsdóttir for providing access
 817 to earthquake locations and magnitude estimates prior to publication. We also thank
 818 Sigrún Hreinsdóttir for providing the 8h GPS time series and Andy Hooper for the pro-
 819 cessed and downsampled interferograms. We thank Jean-Luc Got and an anonymous re-
 820 viewer for their constructive remarks. All data used in this study can be found under
 821 following references [Sigmundsson *et al.*, 2015; Greenfield *et al.*, 2018; Ágústsdóttir *et al.*,
 822 2019]. This research was supported by: NASA under the NASA Earth and Space Sci-
 823 ence Fellowship Program - Grant NNX16AO40H, and NASA ROSES ESI - Grant NNX16AN08G.

824 References

- 825 Ágústsdóttir, T., J. Woods, T. Greenfield, R. G. Green, R. S. White, T. Winder,
 826 B. Brandsdóttir, S. Steinhórsson, and H. Soosalu (2016), Strike-slip faulting dur-
 827 ing the 2014 Bárðarbunga-Holuhraun dike intrusion, central Iceland, *Geophysical*
 828 *Research Letters*, *43*(4), 1495–1503, doi:10.1002/2015GL067423.
- 829 Ágústsdóttir, T., J. Woods, T. Winder, R. S. White, T. Greenfield, and B. Brands-
 830 dóttir (2019), Intense seismicity during the 2014–15 Bárðarbunga–Holuhraun
 831 rifting event, Iceland, reveals the nature of dike-induced earthquakes and
 832 caldera collapse mechanisms, *Journal of Geophysical Research: Solid Earth*, doi:
 833 10.1029/2018JB016010.
- 834 Árnadóttir, P., W. Jiang, K. L. Feigl, H. Geirsson, and E. Sturkell (2006), Kine-
 835 matic models of plate boundary deformation in southwest Iceland derived from
 836 GPS observations, *Journal of Geophysical Research: Solid Earth*, *111*(B7), doi:
 837 10.1029/2005JB003907, b07402.
- 838 Audet, C., and J. E. Dennis Jr (2002), Analysis of generalized pattern searches,
 839 *SIAM Journal on Optimization*, *13*(3), 889–903, doi:10.1137/S1052623400378742.
- 840 Blanpied, M., D. Lockner, and J. Byerlee (1991), Fault stability inferred from gran-
 841 ite sliding experiments at hydrothermal conditions, *Geophysical Research Letters*,
 842 *18*(4), 609–612, doi:10.1029/91GL00469.
- 843 Brandsdottir, B., and P. Einarsson (1979), Seismic activity associated with the
 844 September 1977 deflation of the Krafla central volcano in Northeastern Ice-
 845 land, *Journal of Volcanology and Geothermal Research*, *6*(3-4), 197–212, doi:
 846 10.1016/0377-0273(79)90001-5.

- 847 Carlson, R. L., and C. N. Herrick (1990), Densities and porosities in the oceanic
848 crust and their variations with depth and age, *Journal of Geophysical Research:*
849 *Solid Earth*, 95(B6), 9153–9170, doi:10.1029/JB095iB06p09153.
- 850 Cayol, V., and F. H. Cornet (1998), Three-dimensional modeling of the 1983–1984
851 eruption at Piton de la Fournaise Volcano, Réunion Island, *Journal of Geophysical*
852 *Research: Solid Earth*, 103(B8), 18,025–18,037, doi:10.1029/98JB00201.
- 853 Christensen, N. I., and R. H. Wilkens (1982), Seismic properties, density, and com-
854 position of the Icelandic crust near Reydarfjörður, *Journal of Geophysical Re-*
855 *search: Solid Earth*, 87(B8), 6389–6395, doi:10.1029/JB087iB08p06389.
- 856 Dieterich, J. (1994), A constitutive law for rate of earthquake production and its ap-
857 plication to earthquake clustering, *Journal of Geophysical Research: Solid Earth*,
858 99(B2), 2601–2618, doi:10.1029/93JB02581.
- 859 Drouin, V., F. Sigmundsson, B. G. Ófeigsson, S. Hreinsdóttir, E. Sturkell, and
860 P. Einarsson (2017), Deformation in the Northern Volcanic Zone of Iceland
861 2008–2014: An interplay of tectonic, magmatic, and glacial isostatic deforma-
862 tion, *Journal of Geophysical Research: Solid Earth*, 122(4), 3158–3178, doi:
863 10.1002/2016JB013206.
- 864 Du, Y., and A. Aydin (1992), Three-dimensional characteristics of dike intrusion
865 along the northern Iceland Rift from inversion of geodetic data, *Tectonophysics*,
866 204(1), 111–121, doi:10.1016/0040-1951(92)90273-9.
- 867 Fialko, Y. A., and A. M. Rubin (1999), What controls the along-strike slopes of vol-
868 canic rift zones?, *Journal of Geophysical Research: Solid Earth*, 104(B9), 20,007–
869 20,020, doi:10.1029/1999JB900143.
- 870 Foreman-Mackey, D., D. W. Hogg, D. Lang, and J. Goodman (2013), emcee:
871 the MCMC hammer, *Publications of the Astronomical Society of the Pacific*,
872 125(925), 306.
- 873 Goldberg, D. E., and J. H. Holland (1988), Genetic algorithms and machine learn-
874 ing, *Machine learning*, 3(2), 95–99.
- 875 Goodman, J., and J. Weare (2010), Ensemble samplers with affine invariance, *Com-*
876 *munications in applied mathematics and computational science*, 5(1), 65–80.
- 877 Got, J.-L., A. Carrier, D. Marsan, F. Jouanne, K. Vogfjörð, and T. Villemin (2017),
878 An analysis of the nonlinear magma-edifice coupling at Grímsvötn volcano
879 (Iceland), *Journal of Geophysical Research: Solid Earth*, 122(2), 826–843, doi:

- 880 10.1002/2016JB012905.
- 881 Green, R. G., T. Greenfield, and R. S. White (2015), Triggered earthquakes sup-
 882 pressed by an evolving stress shadow from a propagating dyke, *Nature Geoscience*,
 883 *8*(8), 629–632, doi:10.1038/ngeo2491.
- 884 Greenfield, T., R. S. White, T. Winder, and T. Ágústsdóttir (2018), Seismicity of
 885 the Askja and Bárðarbunga volcanic systems of Iceland, 2009–2015, *Journal of*
 886 *Volcanology and Geothermal Research*, doi:10.1016/j.jvolgeores.2018.08.010.
- 887 Guðmundsson, M. T., and Þ. Högnadóttir (2007), Volcanic systems and
 888 calderas in the Vatnajökull region, Central Iceland: Constraints on crustal
 889 structure from gravity data, *Journal of Geodynamics*, *43*(1), 153–169, doi:
 890 10.1016/j.jog.2006.09.015, hotspot Iceland.
- 891 Hainzl, S., S. Steacy, and D. Marsan (2010), Seismicity models based on Coulomb
 892 stress calculations, Community Online Resource for Statistical Seismicity Analysis,
 893 doi:10.5078/corssa-32035809. [Available at <http://www.corssa.org>.]
- 894 Hartley, M. E., and T. Thordarson (2013), The 1874–1876 volcano-tectonic episode
 895 at Askja, North Iceland: Lateral flow revisited, *Geochemistry, Geophysics, Geosys-*
 896 *tems*, *14*(7), 2286–2309, doi:10.1002/ggge.20151.
- 897 Heimisson, E. R. (2019), Constitutive law for earthquake production based on rate-
 898 and-state friction: Theory and application of interacting sources, *Journal of Geo-*
 899 *physical Research: Solid Earth*, *124*(2), 1802–1821, doi:10.1029/2018JB016823.
- 900 Heimisson, E. R., and P. Segall (2018), Constitutive law for earthquake production
 901 based on rate-and-state friction: Dieterich 1994 revisited, *Journal of Geophysical*
 902 *Research: Solid Earth*, *123*(5), 4141–4156, doi:10.1029/2018JB015656.
- 903 Heimisson, E. R., A. Hooper, and F. Sigmundsson (2015a), Forecasting the path
 904 of a laterally propagating dike, *Journal of Geophysical Research: Solid Earth*,
 905 8774–8792, doi:10.1002/2015JB012402.
- 906 Heimisson, E. R., P. Einarsson, F. Sigmundsson, and B. Brandsdóttir (2015b),
 907 Kilometer-scale Kaiser effect identified in Krafla volcano, Iceland, *Geophysical*
 908 *Research Letters*, *42*(19), 7958–7965, doi:10.1002/2015GL065680.
- 909 Hooper, A., B. Ófeigsson, F. Sigmundsson, B. Lund, P. Einarsson, H. Geirsson, and
 910 E. Sturkell (2011), Increased capture of magma in the crust promoted by ice-cap
 911 retreat in Iceland, *Nature Geoscience*, *4*(11), 783–786, doi:10.1038/ngeo1269.

- 912 Hsu, Y.-J., M. Simons, S.-B. Yu, L.-C. Kuo, and H.-Y. Chen (2003), A two-
 913 dimensional dislocation model for interseismic deformation of the taiwan mountain
 914 belt, *Earth and Planetary Science Letters*, *211*(3), 287 – 294, doi:10.1016/S0012-
 915 821X(03)00203-6.
- 916 Inbal, A., J.-P. Ampuero, and J.-P. Avouac (2017), Locally and remotely triggered
 917 aseismic slip on the central San Jacinto fault near Anza, CA, from joint inversion
 918 of seismicity and strainmeter data, *Journal of Geophysical Research: Solid Earth*,
 919 *122*(4), 3033–3061, doi:10.1002/2016JB013499.
- 920 Jónsson, S., H. Zebker, P. Cervelli, P. Segall, H. Garbeil, P. Mouginiis-Mark, and
 921 S. Rowland (1999), A shallow-dipping dike fed the 1995 flank eruption at Fernan-
 922 dina volcano, Galapagos, observed by satellite radar interferometry, *Geophysical*
 923 *Research Letters*, *26*(8), 1077–1080, doi:10.1029/1999GL900108.
- 924 Key, J., R. S. White, H. Soosalu, and S. S. Jakobsdóttir (2011), Multiple melt injec-
 925 tion along a spreading segment at Askja, Iceland, *Geophysical Research Letters*,
 926 *38*(5), doi:10.1029/2010GL046264.
- 927 LaFemina, P. C., T. H. Dixon, R. Malservisi, P. Árnadóttir, E. Sturkell, F. Sig-
 928 mundsson, and P. Einarsson (2005), Geodetic GPS measurements in south Ice-
 929 land: Strain accumulation and partitioning in a propagating ridge system, *Journal*
 930 *of Geophysical Research: Solid Earth*, *110*(B11), doi:10.1029/2005JB003675.
- 931 Larsen, G., and K. Grönvold (1979), Volcanic eruption through a geothermal bore-
 932 hole at Namafjall, Iceland, *Nature*, *278*, 707–710.
- 933 Linker, M. F., and J. H. Dieterich (1992), Effects of variable normal stress on rock
 934 friction: Observations and constitutive equations, *Journal of Geophysical Re-*
 935 *search: Solid Earth*, *97*(B4), 4923–4940, doi:10.1029/92JB00017.
- 936 Marsan, D., and O. Lengline (2008), Extending earthquakes’ reach through cascad-
 937 ing, *Science*, *319*(5866), 1076–1079, doi:10.1126/science.1148783.
- 938 Parks, M. M., E. R. Heimisson, F. Sigmundsson, A. Hooper, K. S. Vogfjörð, T. Ár-
 939 nadóttir, B. Ófeigsson, S. Hreinsdóttir, Á. R. Hjartardóttir, P. Einarsson, et al.
 940 (2017), Evolution of deformation and stress changes during the caldera collapse
 941 and dyking at Bárðarbunga, 2014–2015: Implication for triggering of seismicity
 942 at nearby Tungnafellsjökull volcano, *Earth and Planetary Science Letters*, *462*,
 943 212–223, doi:10.1016/j.epsl.2017.01.020.

- 944 Rubin, A. M. (1993), Tensile fracture of rock at high confining pressure: Implica-
 945 tions for dike propagation, *Journal of Geophysical Research: Solid Earth*, *98*(B9),
 946 15,919–15,935, doi:10.1029/93JB01391.
- 947 Rubin, A. M., and D. Gillard (1998), Dike-induced earthquakes: Theoretical consid-
 948 erations, *Journal of Geophysical Research: Solid Earth*, *103*(B5), 10,017–10,030,
 949 doi:10.1029/97JB03514.
- 950 Ruch, J., T. Wang, W. Xu, M. Hensch, and S. Jónsson (2016), Oblique rift opening
 951 revealed by reoccurring magma injection in central Iceland, *Nature communica-*
 952 *tions*, *7*, 12352, doi:10.1038/ncomms12352.
- 953 Savage, J. C., and R. O. Burford (1973), Geodetic determination of relative plate
 954 motion in central California, *Journal of Geophysical Research*, *78*(5), 832–845,
 955 doi:10.1029/JB078i005p00832.
- 956 Segall, P., A. L. Llenos, S.-H. Yun, A. M. Bradley, and E. M. Syracuse (2013),
 957 Time-dependent dike propagation from joint inversion of seismicity and defor-
 958 mation data, *Journal of Geophysical Research: Solid Earth*, *118*(11), 5785–5804,
 959 doi:10.1002/2013JB010251.
- 960 Sigmundsson, F., S. Hreinsdóttir, A. Hooper, Þ. Árnadóttir, R. Pedersen, M. J.
 961 Roberts, N. Óskarsson, A. Auriac, J. Decriem, P. Einarsson, H. Geirsson, M. Hen-
 962 sch, B. G. Ófeigsson, E. Sturkell, H. Sveinbjörnsson, and K. L. Feigl (2010), Intru-
 963 sion triggering of the 2010 Eyjafjallajökull explosive eruption, *Nature*, *468*(7322),
 964 426–430, doi:10.1038/nature09558.
- 965 Sigmundsson, F., A. Hooper, S. Hreinsdóttir, K. S. Vogfjörð, B. G. Ófeigsson, E. R.
 966 Heimisson, S. Dumont, M. Parks, K. Spaans, G. B. Guðmundsson, V. Drouin,
 967 Þ. Árnadóttir, K. Jónsdóttir, M. T. Guðmundsson, Þ. Högnadóttir, H. M. Friðriks-
 968 dóttir, M. Hensch, P. Einarsson, E. Magnússon, S. Samsonov, B. Brandsdóttir,
 969 R. S. White, Þ. Ágústsdóttir, T. Greenfield, R. G. Green, Á. R. Hjartardóttir,
 970 R. Pedersen, R. A. Bennett, H. Geirsson, P. C. La Femina, H. Björnsson, F. Pál-
 971 son, E. Sturkell, C. J. Bean, M. Mollhoff, A. K. Braidon, and E. P. S. Eibl (2015),
 972 Segmented lateral dyke growth in a rifting event at Bardarbunga volcanic system,
 973 Iceland, *Nature*, *517*(7533), 191–195, doi:10.1038/nature14111.
- 974 Soosalu, H., J. Key, R. White, C. Knox, P. Einarsson, and S. S. Jakobsdóttir (2010),
 975 Lower-crustal earthquakes caused by magma movement beneath Askja volcano on
 976 the north Iceland rift, *Bulletin of Volcanology*, *72*(1), 55–62, doi:10.1007/s00445-

0977 009-0297-3.

0978 Spaans, K., and A. Hooper (2018), Insights into the stress field around Bárðarbunga
0979 volcano from the 2014/2015 Holuhraun rifting event, *Journal of Geophysical Re-*
0980 *search: Solid Earth*, *123*(4), 3238–3249, doi:10.1002/2017JB015274.

0981 Sparks, R., P. Meyer, and H. Sigurdsson (1980), Density variation amongst mid-
0982 ocean ridge basalts: Implications for magma mixing and the scarcity of primitive
0983 lavas, *Earth and Planetary Science Letters*, *46*(3), 419–430.

0984 Sturkell, E., and F. Sigmundsson (2000), Continuous deflation of the Askja caldera,
0985 Iceland, during the 1983–1998 noneruptive period, *Journal of Geophysical Re-*
0986 *search: Solid Earth*, *105*(B11), 25,671–25,684, doi:10.1029/2000JB900178.

0987 Townsend, M. R., D. D. Pollard, and R. P. Smith (2017), Mechanical models
0988 for dikes: A third school of thought, *Tectonophysics*, *703–704*, 98–118, doi:
0989 10.1016/j.tecto.2017.03.008.

0990 Yun, S., P. Segall, and H. Zebker (2006), Constraints on magma chamber geom-
0991 etry at Sierra Negra Volcano, Galapagos Islands, based on InSAR observa-
0992 tions, *Journal of Volcanology and Geothermal Research*, *150*(1), 232 – 243, doi:
0993 <https://doi.org/10.1016/j.jvolgeores.2005.07.009>, the Changing Shapes of Active
0994 Volcanoes.